1990

Diagnostic probes for particle and molecule distributions in laser-generated plumes

Sandra Marshall Kimbrell
Iowa State University

Order Number 9110521

Diagnostic probes for particle and molecule distributions in laser-generated plumes

Kimbrell, Sandra Marshall, Ph.D.

Iowa State University, 1990

U·M·I
300 N. Zeeb Rd.
Ann Arbor, MI 48106

Diagnostic probes for particle and molecule distributions in laser-generated plumes

by

Sandra Marshall Kimbrell

A Dissertation Submitted to the
Graduate Faculty in Partial Fulfillment of the
Requirements for the Degree of
DOCTOR OF PHILOSOPHY

Department: Chemistry
Major: Analytical Chemistry

Approved:

Signature was redacted for privacy.

In Charge of Major Work

Signature was redacted for privacy.

For the Major Department

Signature was redacted for privacy.

For the Graduate College

Iowa State University
Ames, Iowa

1990

TABLE OF CONTENTS

GENERAL INTRODUCTION

Introduction to Laser Microprobe Analysis

Properties of manufactured materials as well as biological and biochemical processes depend on the presence and concentration of trace elements. Thus, the field of trace analysis has gained significant importance in an increasingly technological world. For solid samples, traditional methods of analysis required tedious grinding and complex dissolution steps, losing forever the ability to record information about the spatial heterogeneity. Preparation steps can also cause problems of dilution and contamination. Solid analysis requires microregion sampling with depth capability, high relative and absolute concentration sensitivity, freedom from matrix effects and minimum variation in element sensitivity (1). The electron and ion microprobes provide direct chemical analysis with excellent spatial resolution (2), but they both require low pressure, increasing cost.

Soon after the demonstration of the laser by Maiman in 1960 (3), the utilization of this unique light source to vaporize solid material was demonstrated by Brech and Cross (4). The advantages of laser microprobe analysis (LMA) for solid sampling are:

1) No sample limitations. Lasers can vaporize conductors, insulators, refractory materials, and even liquids. Whereas, the electron and ion microprobes require a thin coating of conductive material to eliminate charging of nonconductive samples which affects the charged beam

(5, 6).

2) Lateral resolution of ~1 μm can be achieved (7). LMA is an excellent way to isolate a small microregion for analysis such as geological inclusions and mineral grains (8).

3) Depth profiling can be done to a resolution ≥0.5 μm (9).

4) At high power densities, $>10^9$ W/cm^2, vaporization selectivity (10, 11) and matrix effects (1) are eliminated. These effects can be problems in arc, spark and electrothermal methods.

5) No or very little sample preparation is needed saving time and avoiding possible contamination from electrodes, reagents and mortars or polishers.

6) LMA is compatible with many different detection methods both optical spectroscopic (9, 12-14) and mass spectrometric (15, 16) detection. Use of a spectrograph, polychromator or mass spectrometer enables simultaneous multielement analysis.

7) Versatile detection schemes can be used to analyze the sample in situ (17), after further excitation in situ (18), or after transport to another excitation source (19).

8) Isotopic abundance can be measured when using mass spectrometric detection (20).

9) Light elements can be detected, which are difficult to detect by electron microprobe (21).

10) High vacuum levels are not required, reducing cost and allowing biological materials to be studied without requiring dehydration.

11) Since the laser energy can be sent over a long distance, due to

its directionality, semi-remote sampling can be done as long as focusing optics can be appropriately placed. Experiments have been done to analyze liquid steel directly (22).

12) Extremely minute amounts of material are actually removed, typically 1 pg to 1 μg (9). In most cases this small damage is tolerable.

13) When using mass spectrometric detection, three modes of laser vaporization can be easily used to generate gas phase species (16). Laser ablation, $>10^9$ W/cm^2, can be used for elemental analysis. Laser desorption, $<10^8$ W/cm^2 can be used to desorb and ionize large nonvolatile organics. At even lower power densities, $\sim 10^6$ W/cm^2, mostly neutrals of the parent molecule are desorbed so selective ionization can be used (23).

In spite of these advantages, laser vaporization suffers from many weaknesses:

1) Poor accuracy. Closely matched standards must be used, but they are difficult to find or manufacture for some samples (8).

2) Poor reproducibility. Problems of reproducibility stem from the dependence of the vaporization process on numerous factors including the laser pulse characteristics and chemical and physical properties of the sample. Relative standard deviations range from 5-30% (24, 25). Normalization methods have been introduced which can improve reproducibility (26-28).

3) The small amount of destruction may not be tolerable in some cases.

4) Continuous sample introduction is difficult due to the pulsed

nature of the vaporization laser and the transfer efficiency of particles.

5) The sample is not atomized completely. This reduces the potential atomic signals and hence degrades detection limit. Particles are observed under relatively mild (29) and severe (30) ablation conditions.

Because of these advantages and disadvantages, LMA is a complementary technique to the other microprobe methods.

As mentioned previously, detection of plume constituents is highly versatile. For atomic species, the most obvious method is observation of elemental emissions directly from the plume which was first shown by Brech and Cross (4) and later developed by Talmi et al. (31). But, the primary spectrum can be plagued with broadened and shifted emission lines and line reversal (14). Auxiliary forms of excitation have been implemented to improve detection, increase emission intensity, narrow spectral lines and lessen line reversal. Most often, cross spark excitation has been used (32, 33), but this method has added problems. Additional ablation of the surface may occur when the electrodes are place too close to the sample. Since some material from the electrodes is also vaporized, contamination or dilution may be a problem (12). Other methods of auxiliary excitation within the plume or after sweeping the vapor into the auxiliary source include radio-frequency discharge (34), microwave plasma discharge (35), direct current argon plasma (36), and inductively coupled argon plasma (19, 37). Atomic emission analysis is especially desirable because of the relative ease of simultaneous multielement detection using a spectrograph with photographic detection or a polychromator with

multichannel photoelectric detection (9).

Atomic absorption (AA), atomic fluorescence (AF), resonance ionization (RI), and chemiluminescence can be used to probe the ground state population of atoms. Mossotti et al. (17) demonstrated atomic absorption directly in the plume using a multiple-pass beam configuration. The plume can be swept into a hot graphite tube (25) or into a flame (38) for auxiliary atomization of particulates. Use of a second laser to stimulate atomic fluorescence was introduced by Measures and Kwong (30). Laser vaporization with laser induced fluorescence has been used to record the gas phase spectrum of Pb_2 (39). This method, combined with supersonic jet expansion, would certainly be useful for spectroscopic analysis of the variety of clusters observed in laser generated plumes. Resonance ionization can be used as a sensitive and selective measurement of atomic number density in the plume (40). Chemiluminescence generation using a reagent buffer gas has recently been demonstrated (41).

Detection of the ionic species by mass spectrometry (15, 16) offers simultaneous detection, isotopic abundance analysis, and excellent sensitivity. Mass detection can be used in the laser ablation mode for elemental determinations (42) or in the laser induced ionization or desorption modes (43) for analyzing large nonvolatile molecules and their fragments.

The coupling of TLC with gas chromatography (TLC-GC) (44) and with mass spectrometry (TLC-LMS) (45) using laser desorption has been recently demonstrated.

LMA has been put to the test for numerous and highly variable samples. Neuninger (46) has reported numerous examples of the use of LMA in forensics. Archeology has taken advantage of the relative nondestructiveness of the technique. Petrakiev et al. (47) identified pigments of dyes from old paintings. The validication of old hatchets was performed by Buravlev et al. (48). Falsification was concluded based on the detection of trace elements. LMA has been applied to the analysis of semiconductors (8) and radioactive products (49), and to the detection of organic compounds on the surfaces of asbestos fibers (50). On the biology front, LMA has been used to analyze individual cells (51). For analysis of large polar bio-organic compounds, Posthumus et al. (52) broke ground by demonstrating molecular ion signals with mass spectrometric detection of oligosaccharides, peptides and nucleosides. These molecules are notoriously difficult to ionize into the gaseous state without fragmentation. Since then, laser desorption of large nonvolatile biologically significant compounds has become a hot topic. Today, molecules at least as large as 250,000 g/mole (53) can be detected using matrix assisted laser desorption/ionization with mass spectrometric detection. The interested reader can find excellent lists of samples analyzed by LMA in References 9, 13, and 15.

Despite the wide use and variable applications of LMA, fundamental understanding of the laser-solid interaction and initiation and growth of the plasma is far from complete.

Overview of Laser-Solid Interactions

The high degree of directionality of laser beams allows them to be focused to near diffraction limited spots. For giant pulsed lasers that deliver the energy in <0.1 μs, focusing produces high photon fluxes well over 10^9 W/cm^2. When a solid surface is exposed to a high photon flux, absorption of the energy and the resultant rapid increase in surface temperature initiates an explosive ejection of hot material from the surface. The plume forms through a complex series of steps which are not thoroughly understood. Understanding the vaporization process is complicated by its dependence on numerous parameters. The vaporization laser wavelength, pulsewidth, spatial distribution, and power density must be taken into account in modelling the process. Sample parameters such as reflectivity, absorptivity, thermal conductivity, heat of vaporization, heat capacity, and surface morphology also influence vaporization. Laser vaporization is generally described for two power density regimes, $<10^8$ W/cm^2 and $>10^8$ W/cm^2. These two regimes produce distinctly different vaporization. A qualitative picture of the processes leading to plume formation follows.

Reflection of some of the incident energy occurs first. The percent reflected depends on the nature of the sample and its surface. Because reflectivity decreases with increasing temperature (54) more laser energy is absorbed at the surface as the surface is heated. The temperature rise at the surface, and hence the change in reflectivity, depends on the power density of the vaporization laser. At $<10^8$ W/cm^2 reflectivity decreases,

but must still be accounted for when calculating the amount of energy absorbed by the sample (55, 56). At higher fluxes, $>10^8$ W/cm^2, reflectivity decreases rapidly and can generally be ignored (57).

For conducting materials, absorption of the laser energy occurs through the conducting electrons. Rapid relaxation of the excited electrons brings about heating, a rapid rise in surface temperature, and thermionic emission. Multiphoton absorption can cause ejection of photoelectrons (14). Insulators and transparent materials are thought to absorb the incident energy at high enough fluxes by a number of mechanisms including by the presence of impurities, surface phenomena, multiphoton ionization and nonlinear effects (58). Once the initial electrons are ejected, the laser energy is absorbed in the insulating material with subsequent heating, evaporation and ionization. In both vaporization regimes, a thin sheet of cold dilute plasma forms near the surface in the initial stages of vaporization. This plasma is regarded as a priming stage for following events (58).

As the surface temperature rises, through more absorption and relaxations, the material in the irradiated spot melts and eventually boils away from the surface. This process is controlled by the thermal conductivity and heat of vaporization of the sample (14). Superheating at the surface at high fluxes, $>10^9$ W/cm^2, can cause ejection of droplets and streams of molten sample material (59).

The initial formation of ions and electrons above the surface becomes important under high power density conditions. The priming plasma also absorbs laser energy decreasing the power reaching the surface for

thermal vaporization. Absorption in the plasma occurs through inverse bremsstrahlung, (free-free transition) (58). The process involves absorption of a photon by an electron-ion system. The electron gains kinetic energy and shares it with the ion in collisions. The increased electron temperature causes increased ionization resulting in increased electron density and increased absorption. If absorption in the plasma builds to a high enough point, as it can with large photon fluxes ($>10^9$ W/cm^2), the plasma becomes opaque (reflective to the incoming radiation) and no laser energy reaches the surface for thermal vaporization (58, 60). The plasma expands, electron density decreases, and laser radiation once again reaches the surface. This pattern becomes self-regulating throughout the length of the laser pulse. Near the end of the laser pulse, the plasma becomes so hot that it can reradiate energy to the sample surface causing more vaporization (60).

At atmospheric pressure, an atmospheric supported shock wave can be produced from the plasma absorption when power density is sufficiently high ($>10^9$ W/cm^2) (61). The shock wave feeds on the laser energy and can shield the surface from radiation. It has been suggested that the extreme heating of a buffer gas through this mechanism can produce complete evaporation of particles and droplets within the hot gas (62, 63).

At an irradiance $<10^8$ W/cm^2, a stream of vapor leaves the surface at a velocity of the order of 10^4 cm/s. For irradiances $>10^9$ W/cm^2, the vapor leaves the surface at velocities of the order of 10^6 cm/s (12).

The radiation from the plume consists of line emission from the

excited ions and neutrals on top of a continuous background from blackbody radiation, bremsstrahlung (opposite of inverse bremsstrahlung), and ion-electron recombination. The intensity of the emission depends on the power density of the vaporization beam. The degree of ionization also depends on the power density. Below 10^8 W/cm^2, the degree of ionization is ~10^{-5}, while at 5 X 10^9 W/cm^2 ionization approaches 100% (15).

The crater that forms is shallow with an annular rim. Adjacent areas show debris from ejected particles or streams of molten material (64).

Diagnostic Techniques for Laser-Generated Plumes

Like other analytical methods, such as the flame, graphite furnace, inductively coupled plasma, and spark, diagnostic methods to improve atomization and understanding of the vaporization processes are needed for the laser microprobe. But, the plume presents unique difficulties that must be overcome. The plume is small (~1mm-1cm; expansion rate depends on power density and pressure of surrounding gases), highly transient, and dynamic. The atomic population lasts ~300 μs at atmospheric pressure. The particle population lasts milliseconds. Various experimental approaches have been used in fundamental investigations of laser-generated plumes.

The emissions directly from the plasma can be recorded with streak or high speed framing cameras which provide temporal resolution of 5-10 ns. Colin et al. (65) used a streak camera to measure the rate

of expansion of the luminous plasma front. Frame cameras record the whole plasma with successive exposures. Scott and Strasheim (66) used a framing camera to distinguish between the modes of vaporization based on the modes of laser operation. But emission studies do not allow diagnostics for the ground state populations, and under mild vaporization conditions, emissions are weak.

Bykovskii et al. (67) measured ion energies and angular distributions of ion emissions with a mass spectrometer. Electron densities can be measured using interferometric techniques (68, 69) and Stark-broadening theory of emission lines (70). Electron number density is important because of inverse-bremmstrahlung absorption in the priming plasma and its relationship to the extent of ionization. Colombant and Tonon (71) used a collisional-radiative model to derive ion populations as functions of electron temperature and electron density. Their results demonstrated that the most prominent ion stage observed from the emission spectrum is a good guide to the temperature in the plasma. Galanti and Peacock (72) used absolute measurements of recombination continua to calculate the electron temperature (T_e), the electron number density (n_e), and ion densities ($n(C^{5+})$ and $n(C^{6+})$) assuming a Maxwellian velocity distribution. A variety of methods is available for temperature measurements, e.g., relative intensity of various spectral lines (73).

Laser beam deflection has recently been introduced as a universal diagnostic tool for ejected material (74). The deflection of a probe laser beam by the refractive index gradient from the expanding plume can be a measure of the amount of material removed, the vertical drift speed,

and the angle of plasma expansion.

Laser-enhance ionization (LEI) (75, 76) and atomic absorption (77) have been used to interrogate the initial moments of the laser plasma. Both methods showed the extreme pressure broadening of the absorption lines due to the high density of the plume in the early stages of development.

Spatial maps of atomic (78) and dimer (79) concentrations in laser-generated plumes based on absorbance measurements using an expanded laser beam and a vidicon camera have been demonstrated. Temporal resolution is determined by the gating of the probe beam.

Most of the diagnostic techniques used, with the obvious exception of photographic methods, do not provide spatially and temporally resolved information for a single vaporization event. Typically, a series of plumes are generated and the probed region is changed incrementally for each laser shot to provide spatial information or a delay time is used to record temporal information. Laser vaporization is notorious for shot-to-shot variability, so construction of spatial and temporal maps based on a series of plumes at best provides an average picture.

There is a great need for an imaging system that provides high spatial and temporal resolution for following transient events. Such a system has recently been demonstrated (80, 81). The new imaging system is based on the ability of an acousto-optic deflector to repeatedly scan a laser beam at high speed while maintaining good spatial resolution. Combining the deflector with a fast waveform digitizer enables one to obtain spatially resolved information continuously over a relatively long

period of time with good temporal resolution for recording single events. The imaging system has the potential to allow the systematic study of the influence of the parameters governing laser vaporization.

Imaging Based on Acousto-optic Laser Beam Deflection

The interaction of sound waves and light in a transparent medium, acousto-optics (A-O), is an effective way of amplitude-modulating, deflecting, or shifting the optical frequency of laser light. These devices have found their way into our everyday lives, e.g., in laser scanners at the supermarket checkout counter and as an integral part of CD players.

High frequency sound waves launched into a transparent material via a piezoelectric transducer produce a periodic change in the refractive index of the material. The sound waves essentially produce a grating that is able to diffract incident light. The amount of light diffracted depends on the power in the acoustic wave. A brief description of the operation of acousto-optics in the Bragg regime and their usefulness as laser beam scanners for imaging is given here.

Figure 1 shows a schematic of the operation of an A-O in the Bragg regime, hence the term Bragg cell for these devices. A modulated voltage applied to the piezo-electric transducer, bonded to the transparent medium, induces vibrations in the transducer. These vibrations are in turn launched into the transparent medium causing a refractive index grating. The sound wave of frequency F, travels in the medium at a

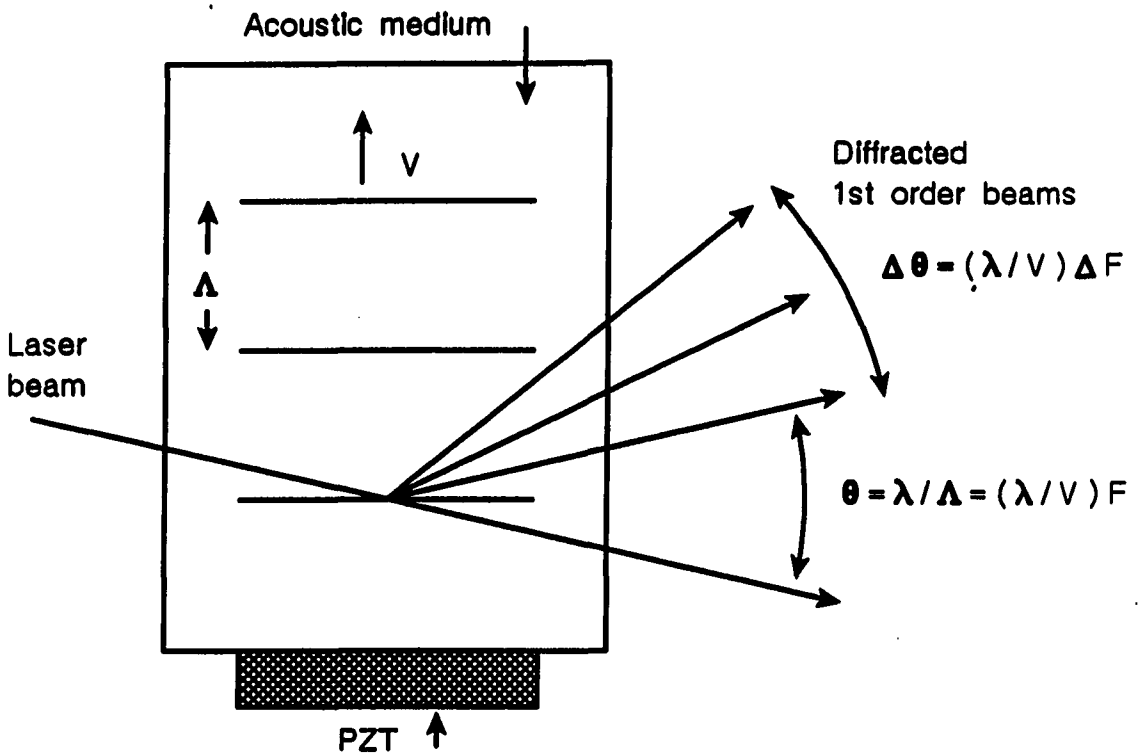

Figure 1. Acousto-optic beam deflector: PZT, piezoelectric transducer; Λ, wavelength of sound in the acoustic medium; V, velocity of sound in the medium; θ, angle of deflection of the 1st order beam from the 0th order; λ, wavelength of the laser beam; F, frequency of the acoustic wave

velocity, V. The sound wavelength, $\Lambda = V/F$, in the medium is analogous to the spacing in a grating. A laser beam, of wavelength λ, properly aligned with respect to the sound waves undergoes diffraction. The deflected beam is separated from the undeflected beam by the angle θ (the Bragg angle = $\theta/2$). If the acoustic frequency is changed by ΔF, then the angle of deflection changes by $\Delta\theta$. In this way, Bragg cells can be used to repetitively and linearly scan a laser beam by modulating the acoustic frequency. The laser beam can thus be linearly deflected through an angle proportional to the change in the acoustic frequency at a linear scan rate equal to the modulation frequency. A thorough discussion of the various parameters which control the performance of the Bragg cell is given by Lekavich (82).

An important figure of merit for A-O beam deflectors is the number of resolvable spots, N, projected on a screen at an arbitrary distance from the device. Resolution is given by the following equation:

$$N = \frac{T - \tau}{T} * \frac{\tau \Delta F}{\alpha} \qquad (1)$$

T: period of the modulation frequency;

τ: time required for sound to cross the diameter of the light beam = laser beam diameter/acoustic velocity;

ΔF: frequency bandwidth;

α: constant related to the amount of overlap between adjacent spots. Values range from 1.17 to 1.66.

Bragg cells are available that provide 1000 resolvable spots at scan rates of 20 spots/μs.

In linear scanning applications, a frequency gradient of θ_{max}/T (θ_{max} is the maximum deflection angle) is produced across the optical aperture. The gradient acts like a cylindrical lens of fixed focal length ($fl = VT/\theta_{max}$) either converging or diverging the diffracted light beam, depending on the sweep direction. Thus, bidirectional scanning cannot be done if this effect is significant. This effect is insignificant at slow scan rates, but at the scan rates that are sometimes used for imaging fast events such as the laser-generated plumes, the effect is important and must be accounted for in the optics alignment.

To use the deflectors in imaging laser-generated plumes, the probe laser beam is sent through the Bragg cell. The scanning 1st order beam is then focused at the plume while the zeroth order and other orders are blocked. The scanning probe beam stimulates absorption, fluorescence, or scattering from the appropriate plume constituents. The resulting signals are focused onto a photoelectric detector to record the signal intensity. In this way, spatial resolution is encoded as temporal signals from the detector.

The plumes can be imaged in one or two dimensions. The second dimension is created by sending the first order beam of one deflector into a second Bragg cell which then scans the beam orthogonal to the first. The resulting deflected laser beam linearly moves through a two dimensional region at a rate proportional to the modulation rates of the two deflectors.

This imaging system has been used to record one-dimensional images of Na (80) and particle (29) distributions in laser-generated plumes.

Two-dimensional imaging of the plume was used to record Na and Pb_2 distributions (81).

The work presented in this thesis uses this imaging system to record spatial and temporal distributions of particle sizes, Sections I and II, in laser generated plumes. Incomplete vaporization of particles represents a loss of atomic signal and thus a degradation of detection limit. If the percent vaporized from shot-to-shot is not consistent, then precision suffers. The determination of the size distribution both spatially and temporally may aid fundamental interpretations of the vaporization process. It should also assist in studies of efficient particle transfer for systems where the plume is swept into auxiliary vaporization sources. First, an introduction to other attempts at particle size measurements in laser-generated plumes will be given. A short introduction to light scattering, the method of choice in the studies presented in this thesis for particle size measurements, will also be given.

The last section of this thesis reports the demonstration of the imaging system to map the desorption process of large nonvolatile organic molecules. Most studies of laser desorption have used mass spectrometric detection. Fundamental studies of the desorption of such molecules in situ should be useful for improving understanding of the desorption process and fragmentation of the molecule.

Particle Size Measurements in Laser-Generated Plumes

Other attempts at particle sizing in plumes generate one average value or do not provide temporal and spatial measurements in situ. Rohlfing (83) determined a rough average size of carbon particles generated from a graphite rod using the second harmonic, 532 nm, of a Q-switched Nd:YAG laser for ablation at ~3 X 10^8 W/cm^2. He fit the emissivity spectra of the hot carbon particles to the theoretical Planck blackbody equation. Rohlfing reported an average size of ~0.06-0.11 μm in radius.

Arrowsmith and Hughes (84) measured particle sizes from the ablation of metals using the fundamental output, 1064 nm, of a Q-switched Nd:YAG laser at ~10^{11} W/cm^2. They attempted to determine the source particle distribution by impacting the plume onto a glass slide placed close to the plume, with subsequent analysis by scanning electron microscopy (SEM). They found many particles <0.25 μm in radius and some >2.5 μm. This method may give larger values from coalescence of particles while on the surface of the slide. The authors also measured particle sizes after sweeping the plume into a particle counter which determines size based on light scattering; again coalescence can lead to larger sizes. They found a size distribution peaking at <0.1-0.15 μm, and on the larger side falling off rapidly to 0.25 μm. A more complete picture can only be developed if the measurements are recorded with spatial and temporal dependence in situ in real time.

The area of particle size analysis has recently been reviewed

(85). Some sizing methods require the extraction of the particles with analysis by a system which separates sizes by physical means. Of the numerous methods available for particle size analysis, optical methods are the most applicable for following small transient events due to the nonintrusive nature of light and the ease of obtaining high spatial resolution with lasers. Various optical measurements can be recorded which reflect particle size such as angular light scatter intensities, color intensities, turbidity, photon correlation spectroscopy, and Fraunhofer diffraction (86). The methods used in this research are based on light scattering.

Introduction to Light Scattering

The intensity and polarization of scattered light by small spherical particles is a complicated function of the wavelength, particle size, refractive index, and scattering angle. Lord Rayleigh (87) solved the simplified problem of scattering by particles much smaller than the wavelength. Gustav Mie (88) formulated the solution to the general problem of light scattering by homogeneous spheres of arbitrary size. There have been a great number of significant contributions to scattering theory from individuals prior to these men and since them. A good historical perspective can be found in Logan (89). The complete theories are thoroughly presented in a number of excellent texts such as Stratton (90), van de Hulst (91), and Kerker (92). To understand the terminology used in scattering theory we must first orient ourselves in

the scattering coordinate system. Figure 2 shows the coordinate system for light scattering. The incident XZ-plane polarized light propagates along the Y-axis. The scattering center is at the origin. The plane of observation, or scattering plane, is defined by the direction of propagation of the incident and scattered light. Typically, the scattered light is observed in the XY-plane, ϕ=90°.

When a plane wave of randomly polarized light is incident on an isotropic spherical particle of arbitrary size, the light scattered at an angle θ with respect to the forward direction of incident light is composed of two incoherent plane polarized components whose planes of polarization are mutually perpendicular. The scattered light which has its plane of polarization perpendicular to the plane of observation is called the vertical or perpendicular component (I_V). The scattered light which is polarized in the plane of observation is called the horizontal or parallel component (I_H). A scattering diagram is often constructed which reflects the intensities of the vertical and horizontal components with respect to θ for a chosen plane of observation. The diagram is often used for particle size measurements, but it requires many measurements at multiple angles. Stringent requirements must be met for the theoretical scattering equations to hold true. There must only be single point scattering. This generally exists when the transmittance of the probe beam is greater than 90% (91). For transmittance in the range 90%-74%, a correction for double scattering may be necessary. For less transmittance, the full complexities of multiple scattering must be used in the model. The scatterers must be isotropic, not optically active, and

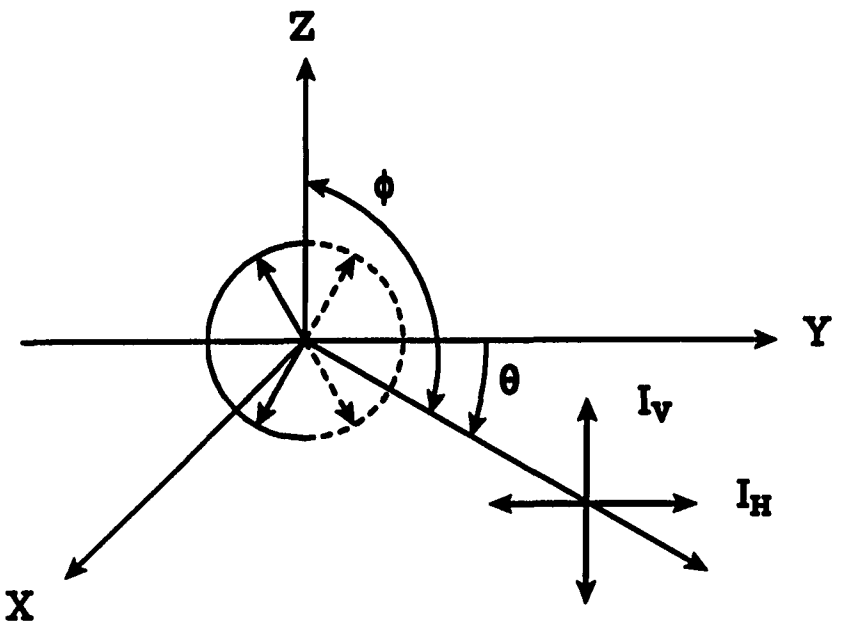

Figure 2. Scattering coordinate system. Incident light is plane polarized in the XZ-plane and travels along the Y-axis. The scatterer has its center at the origin. Direction of the scattered wave is defined by the polar angles θ and ϕ and its components are given by I_V and I_H as shown for observation in the XY-plane

spherical. Scattering equations for anisotropic particles and for particles of other shapes are continually being developed.

When plane polarized light of unit intensity is incident on a particle which is much smaller than the wavelength, the intensity of the light scattered into an angle θ is given by the following equation:

$$I_\theta = \frac{8\pi^4 r^6}{R^2\lambda^4}\left(\frac{m^2 - 1}{m^2 + 2}\right)^2\left(1 + \cos^2\theta\right) \qquad (2)$$

r: radius of the particle;

R: distance between the point of scattering and the point of observation;

λ: wavelength of incident light;

m: complex relative refractive index of the particle to its medium ($m = n_{particle}/n_{medium}$);

θ: angle of scattering with respect to the forward direction of incident light;

This is the well known scattering problem solved by Lord Rayleigh (87). Light scattered at 90° is completely vertically polarized. At other observation angles, the scattering diagram follows a well known pattern that is uniform in intensity at all angles of θ for the vertical component and symmetrical about 90°, dumbbell shaped, for the horizontal component. The $\cos^2\theta$ term gives the horizontal component and the unity, 1, term gives the vertical component.

Particle size analysis in the Rayleigh regime requires measurement of a quantity linear with respect to particle volume such as refractive

index and a quantity that is quadratic with respect to particle volume such as total scattering. A well calibrated system that records total scattering and extinction provides sizing in the Rayleigh regime (91). Particles in the Rayleigh regime and larger are expected for ablation conditions. In fact laser ablation has been developed as a particle generator (93). Rayleigh sized particles would be more easily vaporized and transported than larger, Mie sized ones. Measurement of the larger particles in the plumes is more interesting because they can reflect a major fraction the vaporized material (84).

Equation 2 is not valid for particles much larger than the incident wavelength of light. This restriction assures that each particle has a uniform internal field induced in it when the incident wave passes through the particle. The equation does not take into account the amplitude of light refracted two or more times within the same particle (94). Thus the limits for Rayleigh scattering are: $\alpha << 1$ and $|m\alpha| << 1$ ($\alpha=2\pi r/\lambda$) (91). As particle size increases relative to the wavelength, light scattered at 90° becomes less than 100% polarized. The scattering diagrams become more complicated with multiple maxima and minima for both scattering components. This is the basis of size measurements in the Mie regime. Particle size measurements in the Mie regime range in complexity from mapping the entire scattering diagram to counting the number of maxima and minima in the diagram for the components to simple two point measurements (95, 96). The methods that require many measurements are not applicable to transient events such as laser generated plumes due to the dynamic nature of the plume and data acquisition rates.

The polarization ratio, the ratio of the two orthogonal components of scattered light at any angle, and the dissymmetry ratio, the ratio of one of the components of scattered light at two angles symmetrical about 90°, are simple two point measurements that can be used to measure particle size (95, 96). By using a ratio, the influence of number density and incident intensity can be conveniently eliminated. Application of these methods for particle size analysis in laser-generated plumes is demonstrated in this thesis in Sections I and II.

SECTION I

PARTICLE SIZE MEASUREMENTS IN LASER GENERATED PLUMES USING THE POLARIZATION RATIO OF SCATTERED LIGHT

INTRODUCTION

When a high powered pulsed laser is tightly focused onto the surface of solid material, absorption of the laser energy brings about a dramatic increase in the surface temperature and in the temperature of the gases (if any) immediately above the surface. Eventually a hot plasma, plume, of material is ejected from the surface (1). The plume can consist of ions, atoms, molecules, clusters and even particles.

Laser microprobe analysis (LMA) is a potentially powerful analytical tool for the study of elemental concentrations in solids providing good lateral and depth resolution. Detection schemes for LMA include mass spectrometrometric (2, 3) and various optical spectroscopic techniques (4, 5). Most of the methods for analysis of plume constituents rely on the atomization or ionization of the blow-off material. The presence of particles, if not completely atomized by subsequent forms of excitation, reflects a loss in potential signal and hence a degradation of detection limit. Even with auxiliary excitation to atomize the particles, the particles can be lost in the transport process. Studies have been conducted on the spatial and temporal distributions of atoms, molecules, and particles in the laser generated plumes (6-10). As a result of these studies, a sputtering mechanism has been proposed (8) as a major pathway for free atom formation.

Clearly, the ability to record spatial and temporal distributions of particle sizes in individual plumes in real time will be useful for optimization of the ablation conditions for complete atomization and for

improving our understanding of laser-solid interactions and plume formation. The use of acousto-optic deflection of a probe laser beam in one (7) and two (9) dimensions has been demonstrated to be a useful imaging technique to obtain spatial and temporal maps of atomic (7, 9), molecular (9) and particle (10) populations in a single laser-generated plume.

Numerous techniques have been developed for particle size analysis. This area has recently been reviewed (11). Sizing methods abound, but the plume limits us to methods that can be used in situ with a small highly transient system. All of the measurements which need to be recorded must be done on a microsecond time scale and with micrometer spatial resolution. Of the sizing methods available, light scattering is most promising for following small highly transient events. The majority of light scattering methods require multiple measurements, so a steady state system is usually required, but there are two methods that require only two measurements. The methods are the polarization ratio method and the dissymmetry ratio method. Both methods have the advantage of using ratios which account for variations in incident light intensity and in particle concentrations.

The polarization ratio method is demonstrated here for mapping copper particles in laser generated plumes. This method is the most straightforward of the two and it is the easiest to implement. Only two measurements need to be recorded, the horizontal and vertical components of the scattered light at a set observation angle. Comparison of the experimental ratio to the theoretical values leads to the particle size.

THEORY

Stringent requirements must be met for the theoretical scattering equations to hold true. There must only be single point scattering from particles of homogeneous size. Scatterers must be isotropic, not optically active, and spherical. An in-depth discussion of light scattering by particles can be found elsewhere (12, 13). The experiment is based on the Mie Theory (14) for light scattering by spherical particles. When plane polarized light of arbitrary polarization and unit intensity is incident on a particle which has a radius approximately equal to the wavelength, then the intensity of the scattered light is given by the following equation:

$$I_\theta = \frac{\lambda^2}{8\pi^2 R^2}(\iota_1 + \iota_2) \qquad (1)$$

θ: angle of observation with respect to the forward direction of propagation of incident light;

R: distance from the scattering center to the point of observation;

λ: wavelength of light;

ι_1: scattered light that has its electric vector perpendicular to the plane of observation;

ι_2: scattered light that has its electric vector in the plane of observation;

The plane of observation is defined by the direction of observation and the direction of propagation of the incident light. The angular

distribution functions, ι_1 and ι_2, are complicated function of α, θ, and m. They are proportional to the intensities of the two incoherent plane polarized components which make up the scattered light. The term α is typically referred to as the size parameter; it is the ratio of the circumference of the particle to the wavelength of incident radiation, $\alpha=2\pi r/\lambda$. The term m is the relative refractive index of the particle to its medium, $n_{particle}/n_{medium}$. The wavelength in the medium is used in the calculations. The complex refractive index, real and imaginary parts, must be used in the calculations of ι_1 and ι_2. The full mathematical definitions of ι_1 and ι_2 can be found elsewhere (12, 15, 16).

The polarization ratio, ι_2/ι_1, is a simple two point measurement that can be used to measure particle size (17, 18). In general this ratio varies irregularly with α, but for values of α in a limited range above the Rayleigh regime and for angles near 90°, the ratio is single valued with respect to α. A plot of theoretical values of the polarization ratio with respect to the size parameter, α, is constructed for each set of conditions (m,λ,θ). Experimental ratios are compared with theoretical values off the curve to determine particle size. If the ratio is outside of the monotonic region, then difficulties arise in assigning a value for the radius due to the irregularities in the theoretical curve.

EXPERIMENTAL

The instrumental setup is shown in Figure 1. The probe laser was the 488 nm output of an argon ion laser (Control Laser, Orlando, FL, Model 554A). The 60° prism, PR, dispersed the wavelengths of the laser output, and the 488 nm line was isolated at the aperture, A. The probe beam was ~3 mm in diameter when it entered the acousto-optic deflector, AOM (Intra Action, Bellwood, IL, Model ADM-150 with DE-150 driver). Full detail is given elsewhere on the operation of Bragg cells (AOD) as laser scanners (7, 9).

An asymmetric triangular waveform of 10 kHz from a waveform generator (Wavetek Corp., Model 162) was input into the AOD rf driver to control the deflection angles and scan rate. The scan was essentially unidirectional with a reset time of ~5 μs. A 50 cm focal length spherical lens, L_1, focused the scanning probe beam at the center of the plume. The laser beam was scanned vertically for a distance of 4.5 mm parallel to the vaporization line at a rate of 10 kHz, for 100 μs temporal resolution. The scan began approximately 1 mm above the sample surface. Spatial resolution was measured by placing a grid at the focal plane and measuring the transmitted beam with a photodiode (Hamatsu, Middlesex, NJ, model S1790-01). Spatial resolution was 42 spots/cm. Maximum spatial resolution was not utilized in this setup. A beam stop (to block the transmitted beam) or a photodiode (to measure transmission) was placed at the exit from the plume. Average power of the probe beam at the plume region was ~50 mW.

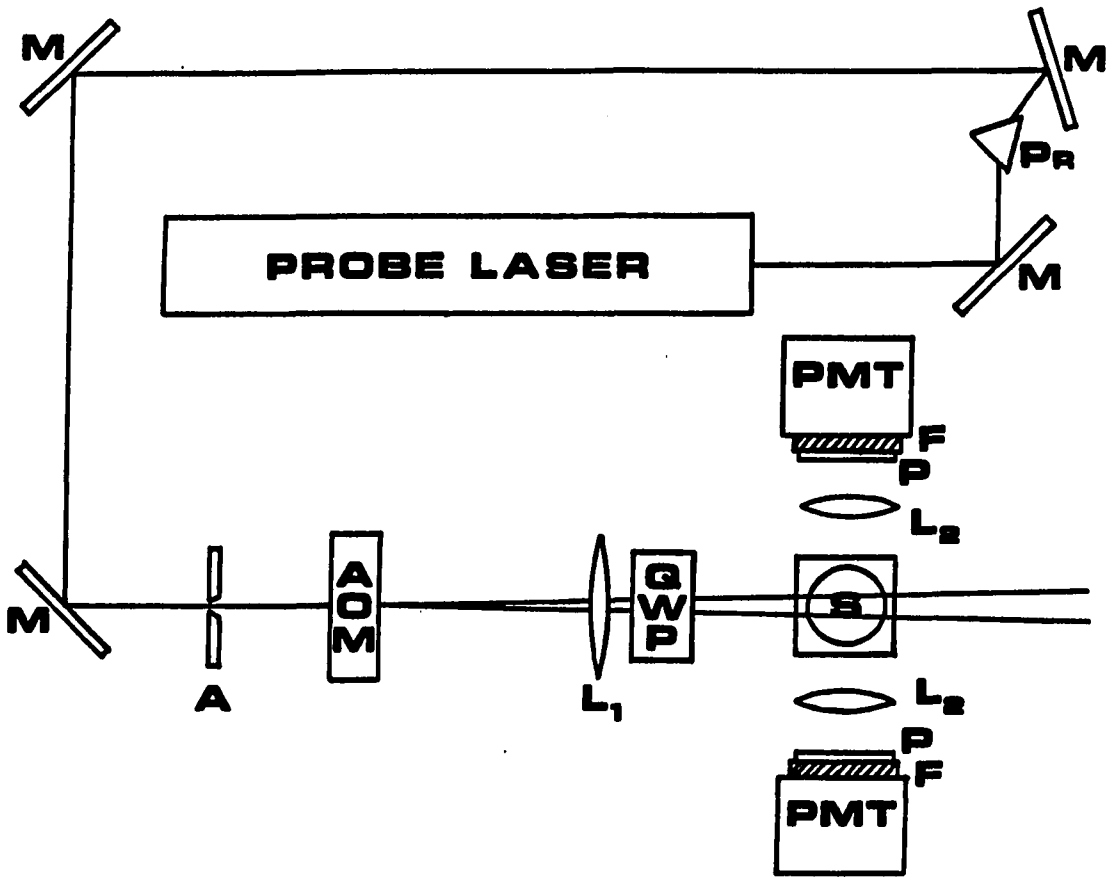

Figure 1. Experimental arrangment for the determination of polarization ratios of scattered light in laser-generated plumes: PROBE LASER, Argon ion laser; M, mirror; PR, 60° prism; A, aperture; AOM, acousto-optic modulator; L_1, 50 cm f.l. spherical lens; QWP, quarter wave plate; S, vaporization cell; L_2, 4 cm f.l. spherical lens; P, polarizer; F, 488 nm line filter; PMT, photomultiplier tube

The argon ion laser beam is vertically polarized, but the scattering method requires random polarization to generate both scattering components. The electric field of the incident light must have equal probability in the vertical and the horizontal directions. A quartz quarter wave plate, QWP, was placed after the lens, L_1, to create "natural" light of equal horizontal and vertical components. The resultant beam was actually elliptically polarized at 45° which will satisfy the requirement. The polarization of the beam was checked by placing a camera polarizer (Photographic Research Organization, Inc., Fairfield, CT) after the QWP. The transmitted beam was detected by a photodiode. The intensity at 0°, 45°, 90°, and 135° polarization was measured to determine the polarization of the resultant beam. The plane of observation was a plane parallel to the plane of the optical table.

The scattered light was collected and focused onto the photocathodes of the photomultiplier detectors, PMT (RCA, Lancaster, PA, Model 1P28), by 4 cm focal length spherical lenses, L_2, placed 8 cm from the scattering region for 1:1 imaging. The diameter of the lenses was 2.54 cm, for a collection angle of 18°. The imaged light passed through a camera polarizer, P, and a 488 nm line filter, F, (Corion Corp., Holliston, MA, Model P1-488) to reduce emission and roomlight background.

The outputs from the detectors were amplified by passing them through separate oscilloscopes (Tetronix, Beaverton, OR, Models 7904 and 7704A) and into separate channels of a waveform digitizer (Data Precision, Danvers, MA, Model 6000/630). The digitizer was operated at 2 MHz with 9 bit resolution, acquiring 200 points/scan. A total of 8 K-bytes of data

were collected in each channel, so each plume was followed for approximately 4 ms. The digitizer was triggered by the SYNCH OUT from the vaporization laser which occurs ~160 ns prior to laser firing. Scattering data were acquired for single shots of the vaporization laser, no averaging of multiple laser plumes was done. After digitization, the data were transferred to a minicomputer (Digital Equipment, Maynard, MA, Model PDP 11/10) through an RS-232 interface. Subsequent analysis was carried out on an AT compatible computer.

The sample cell has been described elsewhere (6). It is an aluminum block with five windows in place for input of the vaporization and probe beams and for the transmission of the probe beam and scattered beams at 90°. A valve in the cell can be used to control the atmosphere. The side windows for viewing scattering were not in place because of the possibility that they might alter the polarization of the scattered light. The other windows were in place to reduce air currents. The scattering data were acquired in air at atmospheric pressure. The sample was copper metal polished with sandpaper to grade 600. The measured reflectivity at 1064 nm was 40%.

The vaporization laser was the fundamental output, 1064 nm, of a Nd:YAG laser (Quantel, Santa Clara, CA, Model VG481) operated at 1 Hz. Typical energy irradiating the sample was 44 mJ per pulse with a 10 ns duration. The vaporization beam was focused onto the surface by a 6 cm focal length cylindrical lens to produce a line ~1 cm X .04 cm. Lower power density was produced by defocusing the ablation laser to a spot ~1 cm X 0.2 cm.

Because a ratio of two signals is desired and separate photomultiplier tubes were used to detect the two polarized components, it was critical to match the gains of the two detectors throughout the imaged area. Photomultipliers have spatially dependent gains and the image is not a point but has a size ~0.45 X 1 cm covering at least 1/2 of the photocathode surface. The detectors were mounted on jacks for ease in positional adjustments. With the polarizers on the detectors set to pass the same polarization of scattered light, slight adjustments were made to the detector positions and the high voltage power supplied to the detectors while observing the scattering signals until the gains were matched between the two detectors throughout the probed area. After subtraction of backgrounds, the signals were matched to within 10% error after averaging 36 successive scans.

Mie scattering functions were evaluated using Fortran programs (Microsoft Corporation, Fortran 77 version 4.01) on a microcomputer (IBM, Boca Raton, CA, PC/AT). Accuracy of the calculations was checked against previously published values. The theoretical polarization ratios for copper with $m = 1.10 - 2.34i$, at 500 nm (13) is shown in Figure 2. The oscillations dampen at larger alphas to a value of 0.66. The oscillations are large enough to limit the monotonic region of the theoretical curve to radii below 0.066 μm ($\alpha = 0.85$). Polarization ratios greater than 1.3 have sizes limited to a range within the first lobe of the theoretical curve, $0.136 < r < 0.188$ μm ($1.75 < \alpha < 2.42$). Figure 3 shows the sum of the theoretical values of the scattering functions at 90°, providing an idea of the change in scattering efficiency with size.

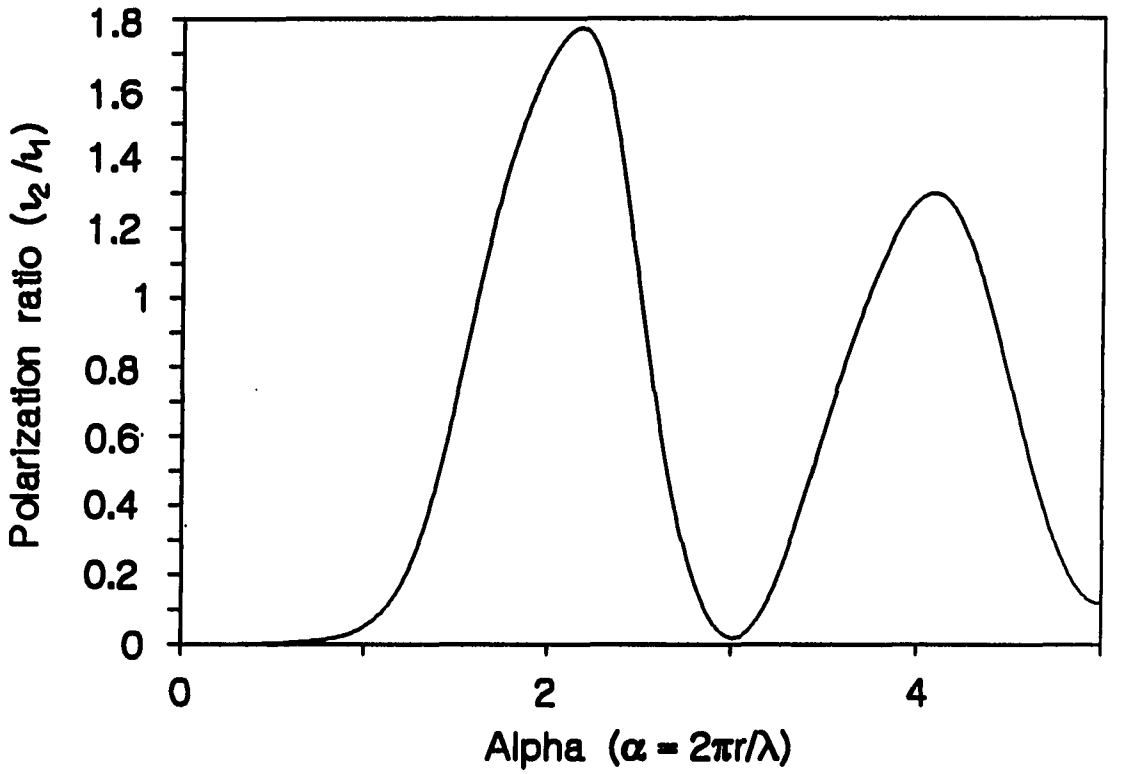

Figure 2. Theoretical polarization ratios at 90° for Cu particles based on m = 1.1 - 2.34i (500 nm)

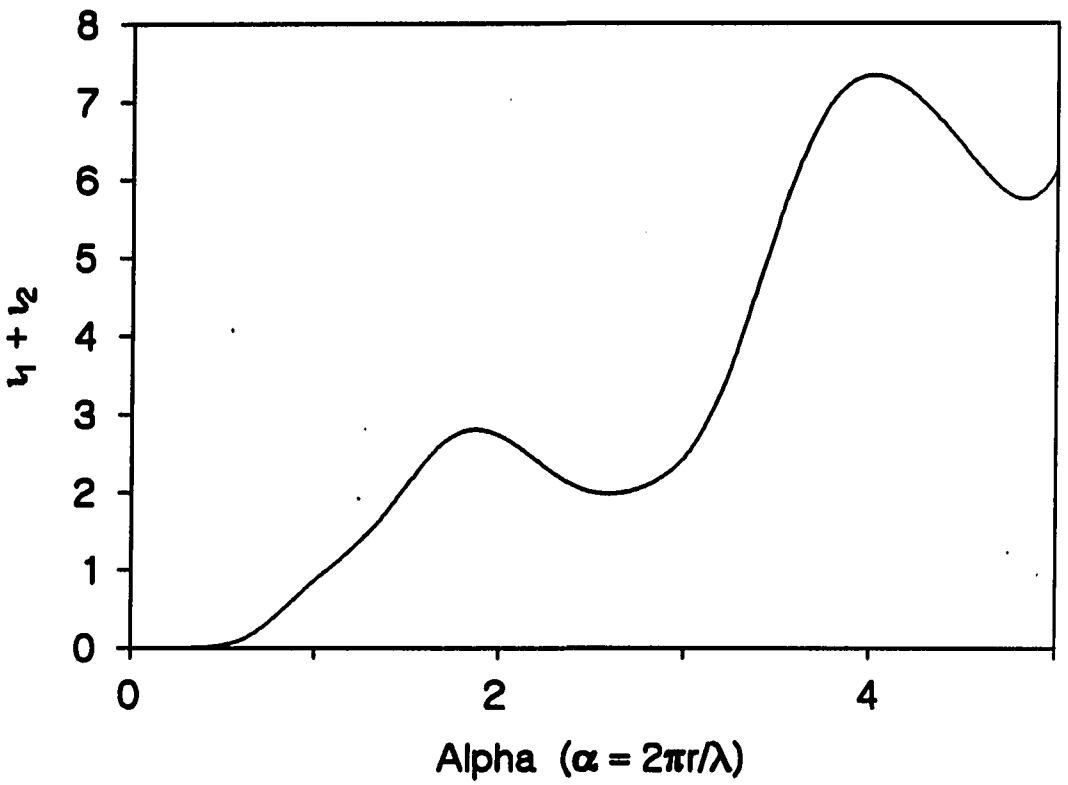

Figure 3. Sum of the theoretical angular distribution functions for scattering at 90° for Cu particles (m = 1.1 - 2.34i; 500 nm)

RESULTS AND DISCUSSION

Spatial and temporal mapping of particles generated from laser vaporization of metallic surfaces has been reported earlier (10). There, total scattering intensity was used to derive relative concentrations. Equation (1) shows that angular dependence, polarization dependence, and particle sizes directly affect the total scattering intensity. The absorption of particles (imaginary part of the refractive index) further complicates the picture. The transmittance of the probe laser beam through the plume was measured to obtain a more reliable picture of the concentration of the particles generated. The experimental procedure used is identical to the one reported earlier for measuring atomic and molecular concentrations (9). In the previous report, transmittance was measured on and off resonance for the atomic or molecular absorption line. No absorption was observed off resonance, showing that particle absorption is negligible. That is, particle concentrations were low. The experiments here involve vaporization regimes where a substantial amount of particles is present. The attenuation in the probe beam is significant even though the wavelength used (488 nm) does not correspond to absorption lines of the Cu atom or its simple clusters. The clusters are large enough that they behave like bulk metal, and attenuation results from both scattering and absorption. A typical concentration map is shown in Figure 4 for a plume formed with the softer focus of the vaporization beam. The normalized scatter signal (at 90°) for the same plume (with no polarizer) is shown in Figure 5. It is clear that at these power levels, the

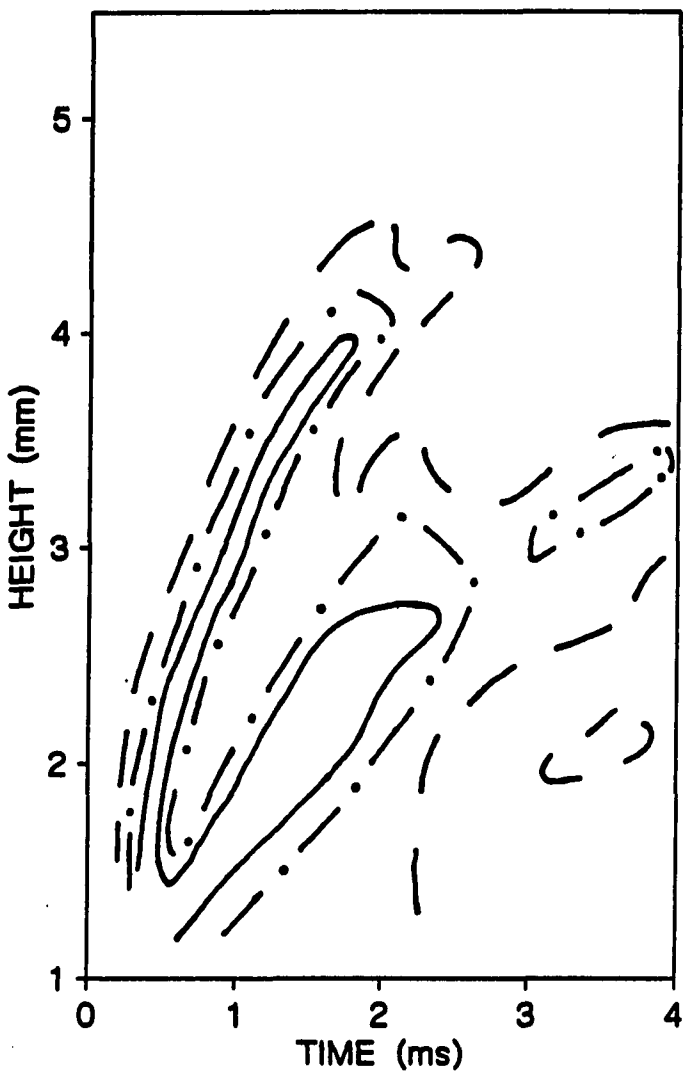

Figure 4. Particle densities as determined from transmission measurements starting at 105 μs after vaporization. Power = 22 MW/cm^2. Contours are for transmittance of 0.89 ——— , 0.92 — • — •, and 0.95 — — —

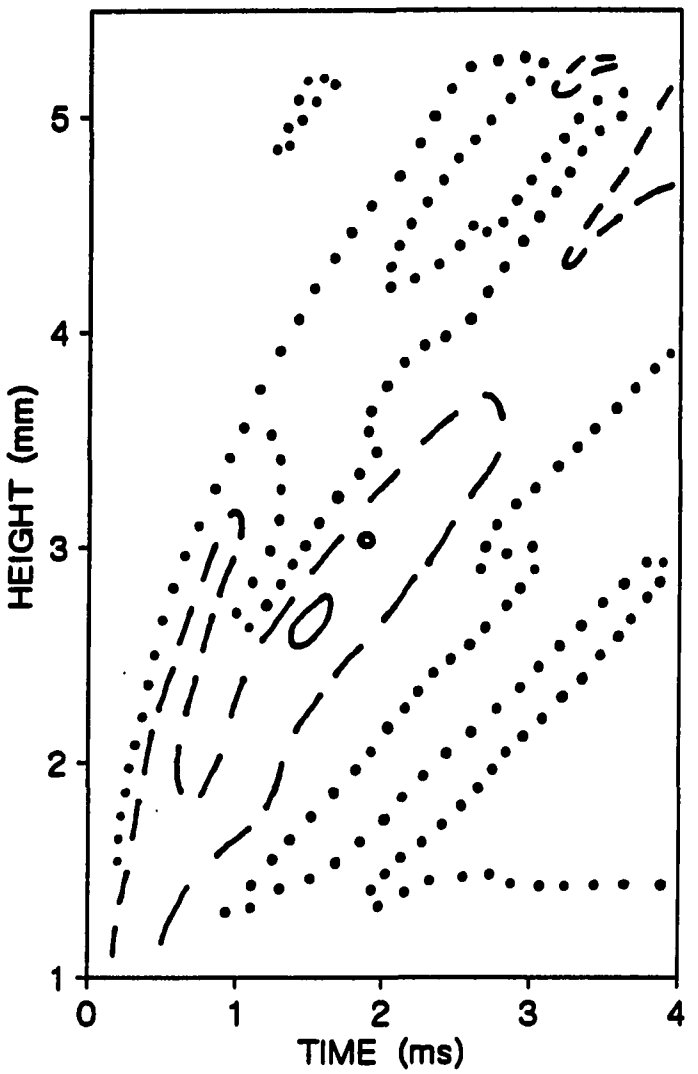

Figure 5. Normalized total scatter collected at 90° for the same plume as that shown in Figure 4. Contours are for relative signals of 1 • • • • , 2 — — — , and 3 ——

particles are generated directly from the metal surface. These move away and diffuse in the observation region as a function of time. The particle density is also fairly smooth, indicating small particles and a gradual vaporization process. At higher power densities, we observe contours that are much more inhomogeneous spatially and temporally, indicating larger particles or groups of particles and a violent vaporization process. These observations are similar to those reported earlier (10). The transmission profile parallels the normalized scatter profile. Lowest transmission occurs in regions of high scatter. There are regions where multiple scattering could be occurring, transmittance < 0.9, which could require the use of theoretical calculations based on double scattering as mentioned in the dissertation introduction for size analysis.

The advantages of the transmission measurements here are that the concentrations are better represented and that one can probe the plume at very early times because of the lack of interference from the intense plasma emission associated with the formation of the plume. The disadvantage is that one does require very high particle densities for transmission measurements. Such densities are typical of laser ablation schemes as a solid probe for, e.g., the inductively coupled plasma emission spectroscopy, but atypical of direct atom or ion generation from surfaces for, e.g., mass spectroscopy.

The polarization ratios (ι_2/ι_1) for copper particles in a plume generated with the softer focus of the vaporization beam are plotted in Figure 6. Since there are only two channels in the waveform analyzer used in this work, the transmission contours and the polarization contours were

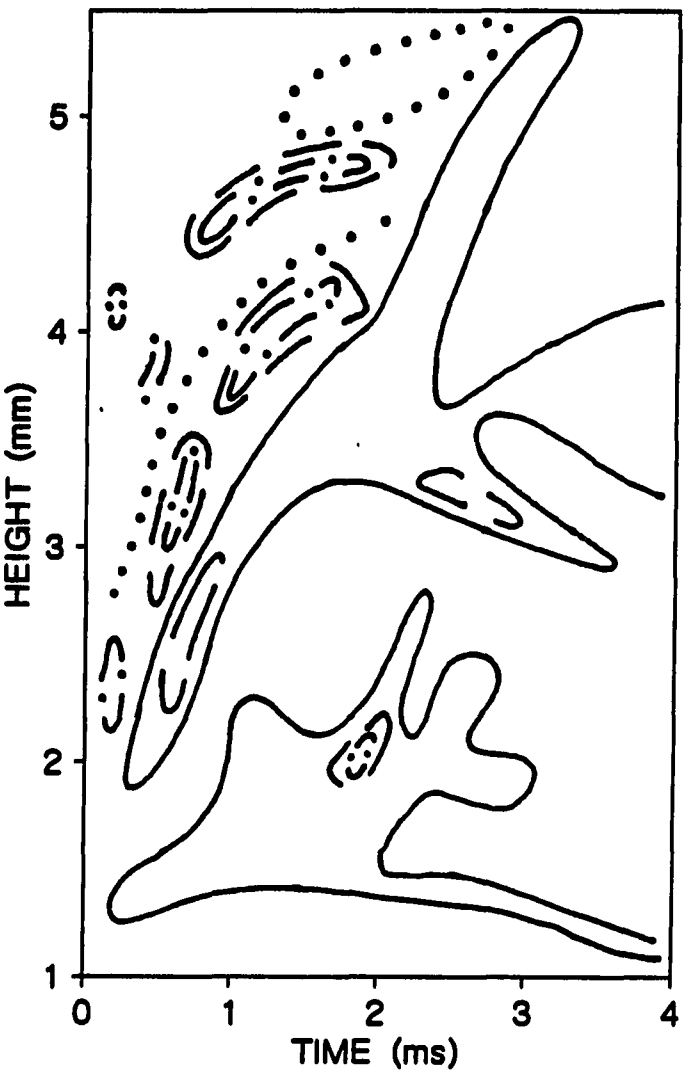

Figure 6. Contour plot of experimental polarization ratios (ι_2/ι_1) for copper particles starting at 28 μs after vaporization. Power = 22 MW/cm^2. Contours are for ratios <0.4 • • • • , 0.8 ——— , 1.1 — — — , and >1.3 — • — •

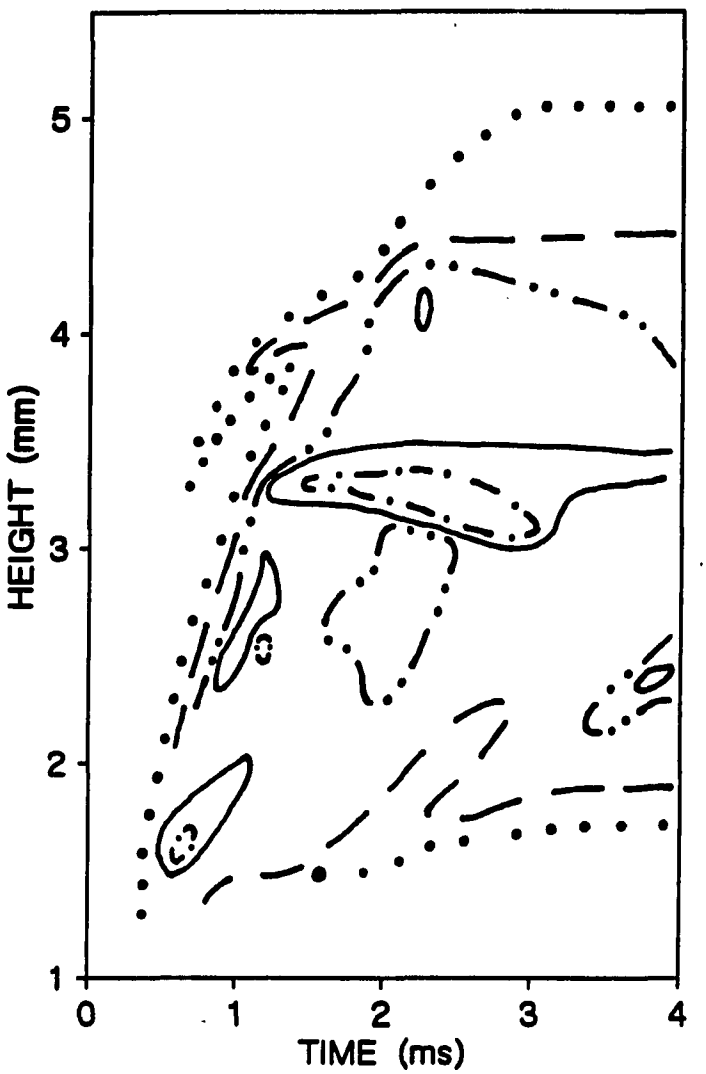

Figure 7. Contour plot of the sum of the experimental scattering signals for the same plume as that shown in Figure 6. Contours are for relative signals of 1 • • • • , 2 — — — , 3 — • • — , 4 ——— , and 5 — • — •

not obtained for the same vaporization event, but the power density at the surface was similar. The general distribution of particle densities, however, is similar at the same laser power used for vaporization. This is further confirmed by the quantity $\iota_1+\iota_2$, shown in Figure 7, from the same raw data in Figures 6. The contours shown in Figures 4-7 are only constructed for regions where the scattering intensities are significant. Interpretation must be made with reference to Figure 4.

To derive exact particle sizes from the data in Figure 6, one needs to make several assumptions. Almost all scattering models rely on having uniform particle sizes. In any particular spatial region at a particular time window, there will be a distribution of particle sizes for these vaporization events. So the best one can do is to determine an average behavior. If the polarization ratios change slowly as a function of space and time, as in some regions in these experiments, the average behavior will be quite meaningful. Most simple scattering treatments also apply only to spherical particles. This is applicable to particles formed via condensation of smaller units or by slow vaporization off the surface, where random orientation can be expected. For violent vaporization events, fragmentation of the bulk material will produce irregular particle shapes. Particle size calculations also require that one is within a certain range of particle diameters for a given model to be valid. The results must therefore be checked for consistency with the chosen model.

The Mie scattering theory is valid for particles with diameters the order of the observation wavelength. Since earlier results (8, 10) show the presence of atoms, dimers, as well as particles the size of the laser

beam waist, it is reasonable to assume that particles in the intermediate sizes are also present. The majority of the experimental polarization ratios are greater than 0.25 corresponding to a radius of 0.098 μm, so the particles observed by this method in these plumes are predominantly larger than 0.098 μm in radius. The greatest number of ratios lies in the multivalued regime between 0.4-0.9. Ratios larger than 1.3 lie in the first lobe of the theoretical curve as noted earlier. In these regions the particle size is in the range 0.136 - 0.188 μm. Ratios greater than 1.3 lie within contours of smaller ratios indicating smoothly changing sizes. Ratios less than 0.4 are only observed at the expanding front of the plume. Behind them are the regions containing the ratios greater than 1.3. Following the regions of largest ratios, we see predominantly ratios in the range 0.4-0.9 which correspond to the regions of strongest scatter. And in comparison to Figure 4, they correspond spatially to the regions of highest concentration. Note, ratios less than 0.4 are not seen in this last region indicating that the sizes in this dominant region do not shift lobes in the theoretical curve. From Figure 7 we see smoothly changing scattering intensities which imply smoothly varying particle sizes. All of these factors taken together support an assumption that the particles observed here are within the first lobe of the theoretical curve. This would put the particles in a range of 0.098 - 0.21 μm. Ratios in the Mie regime are seen early on in time. This shows that one does have particles formed directly at the surface and moving away from it. So, condensation is not the only mechanism for particle formation in these experiments.

In summary, techniques have been demonstrated for mapping particle

concentration (by transmission) and for determining polarization ratios in laser-generated plumes. The polarization ratios provide good estimates of particle size. Simultaneous measurement of the polarization ratios at three angles should be done to avoid ambiguity, but this obviously increases the complexity and cost of the measurement. Good spatial and temporal resolution is achieved. Extension to two-dimensional mapping is straightforward.

REFERENCES

1. Ready, J. F. Effects of High-Power Laser Radiation; Academic: New York, 1971.

2. Conzemius, R. J.; Capellen, J. M. Int. J. Mass Spectrom. Ion Phys. 1980, 34, 197-271.

3. Houk, R. S. In Analytical Applications of Lasers; Piepmeier, E., Ed.; Wiley: New York, 1986; Chapter 18.

4. Dittrich, K.; Wennrich, R. Prog. Anal. Atom. Spectrosc. 1984, 7, 139-198.

5. Piepmeier, E. H. In Analytical Applications of Lasers; Piepmeier, E., Ed.; Wiley: New York, 1986; Chapter 19.

6. Steenhoek, L. E.; Yeung, E. S. Anal. Chem. 1981, 53, 528.

7. Huie, C. W.; Yeung, E. S. Appl. Spectrosc. 1986, 40, 863.

8. Huie, C. W.; Yeung, E. S. Spectrochim. Acta 1985, 40B, 1255.

9. Yappert, M. C.; Kimbrell, S. M.; Yeung, E. S. Appl. Optics 1987, 26, 3536.

10. Huie, C. W.; Yeung, E. S. Anal. Chem. 1986, 58, 1989.

11. Barth, H. G.; Sun, S-T.; Nickol, R. M. Anal. Chem. 1987, 59, 142R.

12. Kerker, M. The Scattering of Light and Other Electromagnetic Radiation; Academic Press: New York, 1969.

13. van de Hulst, H. C. Light Scattering by Small Particles; Dover: New York, 1981.

14. Mie, G. Ann. Physik 1908, 25, 377.

15. Lowan, A. N. Tables of Scattering Functions for Spherical Particles; National Bureau of Standards: Washington, D.C., 1948; A.M.S.-4.

16. Stratton, J. A. Electromagnetic Theory; McGraw-Hill: New York, 1941.

17. Sinclair, D.; La Mer, K. Chem. Rev. 1949, 44, 245-266.

18. Meehan, E. J.; Beattie, W. H. J. Phys. Chem. 1960, 64, 1006.

SECTION II

REAL-TIME PARTICLE SIZE MEASUREMENTS IN LASER GENERATED PLUMES USING DISSYMMETRY RATIOS OF SCATTERED LIGHT

INTRODUCTION

When laser energy is tightly focused, it can vaporize virtually any material while providing good spatial and depth resolution (1). This makes the laser microprobe analyzer (LMA) an excellent tool for solid sampling where often times the analyst is confronted with a wide variety of samples requiring microregion sampling. Absorption of the laser energy at the surface results in a rapid temperature increase at the surface, melting, and eventually boiling (2, 3). The cloud of material ejected from the surface can consist of atoms, molecules, ions and particles.

Analysis of the plume constituents can be accomplished by a variety of methods. The ions are conveniently monitored by mass spectrometry (4). Many optical spectroscopic methods (1, 5) have been employed to monitor the neutral species directly in the plasma or after further excitation in situ or after sweeping the plume into an auxiliary source. Even with the additional excitation steps taken to improve detection, reproducibility is often poor, ranging from 5 to 30% (6, 7). Poor reproducibility can be attributed, in part, to variability in the vaporization process. Numerous factors affect vaporization (2, 3) including the laser pulse characteristics, such as the spatial and temporal characteristics of the pulse, power density, and wavelength. Some of the sample parameters that affect vaporization include reflectivity, thermal conductivity, heat of vaporization, surface roughness, and absorptivity. Normalization methods that use internal standardization have been developed to improve precision (8-10).

Recently, a new imaging method was demonstrated for mapping dynamic, transient events. The method is based on the ability of acousto-optic deflectors to repetitively scan a probe laser beam over a region with good temporal and spatial resolution. Spatial and temporal distributions of atoms (11, 12), molecules (12), and particles (13, 14) in laser-generated plumes have been recorded using this method.

The great majority of methods used for analysis of plume constituents rely on complete atomization or ionization. The particles in the plume have been shown to constitute a major part of the mass removed from the sample under certain conditions (15). This causes a substantial reduction of potential atomic signal for direct analysis within the plume. Although auxiliary excitation has been used to further vaporize particulates, irreproducibility associated with sampling, transport, and recondensation is still present.

The ability to follow the spatial and temporal variations of the particle sizes may improve our understanding of the vaporization process within the plume. Of the numerous methods developed for particle size analysis, light scattering techniques are the most applicable for following transient events such as the plumes.

A new method for determining particle sizes in a single laser-generated plume with good spatial and temporal resolution is reported here. The method is based on the Mie theory of light scattering by spherical particles (16). Previously (14), the polarization ratio of scattered light was used to measure the size of particles in a plume generated from a copper surface. The method presented here uses the

dissymmetry ratio of scattered light. For the system studied here, dissymmetry ratios provide more reliable information compared to polarization ratios. Like the polarization method, only two measurements are recorded, specifically, the intensities scattered for a single polarization at two angles symmetrical about 90°. Experimental ratios are compared to theoretical ones calculated from the Mie equations to determine particle size.

THEORY

The use of light scattering measurements for particle size analysis has been demonstrated in numerous studies (17, 18). The theory is well developed and reviewed in numerous papers and books (19, 20). A general form of the equations for the intensity of light scattered by spherical particles when illuminated by polarized light of unit intensity is:

$$I_{\phi,\theta} = I_V = \left(\frac{\lambda^2}{4\pi^2 R^2}\right) \iota_1 \tag{1a}$$

$$I_{\phi,\theta} = I_H = \left(\frac{\lambda^2}{4\pi^2 R^2}\right) \iota_2 \tag{1b}$$

ϕ: angle of observation with respect to the polarization of the incident light;

θ: angle of observation with respect to the direction of propagation of incident light;

λ: wavelength in the medium;

R: distance from the scattering center to the point of observation;

ι_1: scattered intensity in the direction of propagation perpendicular to the polarization of incident light, ϕ=90°;

ι_2: scattered intensity in the plane defined by the polarization of incident light and its direction of propagation, ϕ=0°;

The angular scattering functions, ι_1 and ι_2, are complicated functions of

α, θ and m, where $\alpha=2\pi r/\lambda$ for a particle of radius r, and m is the relative complex refractive index of the particle to its medium. For absorbing scatterers, the complex refractive index must be used in the evaluation of the functions. At any other observation planes, the scattered light is elliptically polarized and ι_1 and ι_2 are not resolved into distinct components (20, 21). Complete mathematical definitions of ι_1 and ι_2 can be found elsewhere (20, 21). The scattering theory assumes spherical particles, single point scattering, isotropic particles and homogeneous particle size.

The dissymmetry ratio, $\iota_1(\theta_1)/\iota_1(180-\theta_1)$, uses the scattered light of a single polarization at two angles symmetrical about $\theta=90°$. This ratio varies irregularly with α. But for small values of α, the ratio is monotonic with respect to α. A plot of theoretical values of this ratio with respect to α can be constructed for each set of conditions (m,θ,λ). Experimental ratios are compared with theoretical values off the curve to determine particle size. If the ratio is outside of the monotonic region, then difficulties arise in assigning a value for the radius due to the irregularities in the theoretical curve.

EXPERIMENTAL

A schematic of the experimental setup is shown in Figure 1. The probe laser was an argon ion laser (Laser Ionics, Orlando, FL, 554A). The output was chosen to be vertically polarized, and the 488 nm line was used as the probe wavelength. Anamorphic optics were used to shape the probe laser beam into a line and focus it into the acousto-optic deflector (Intra Action, Bellwood, IL, ADM-150). An asymmetric triangular waveform of 50 kHz from a waveform generator (Wavetek Corporation, San Diego, CA, Model 162) was input to the rf deflector driver (Intra Action, Bellwood, IL, DE-150) to control deflection angle and scan rate. Use of acousto-optic deflectors as laser beam scanners for plume diagnostics has been demonstrated previously with a thorough discussion of design consideration (11, 12). The deflected first order beam was focused at the plume position using a 50 cm focal length spherical lens, S_1. The probe beam was deflected vertically at 50 kHz to span a region 5.5 mm above the sample beginning ~0.5 mm above the sample surface. Spatial resolution at the plume of 55 μm was confirmed by placing a grid at the focal point and measuring the intensity of the transmitted beam with a photodiode (Hamamatsu, Middlesex, NJ, Model 21790-01). The average power of the probe beam at the plume region was ~50 mW.

The scattered radiation was collected at 45° and 135° and imaged onto the photocathodes of the photomultiplier tubes (RCA, Lancaster, PA, 1P28 and Hamamatsu, Middlesex, NJ, R928), PMT, using 7.5 cm focal length spherical lenses, S_2, of 2.54 cm diameter placed 15 cm from the plume for

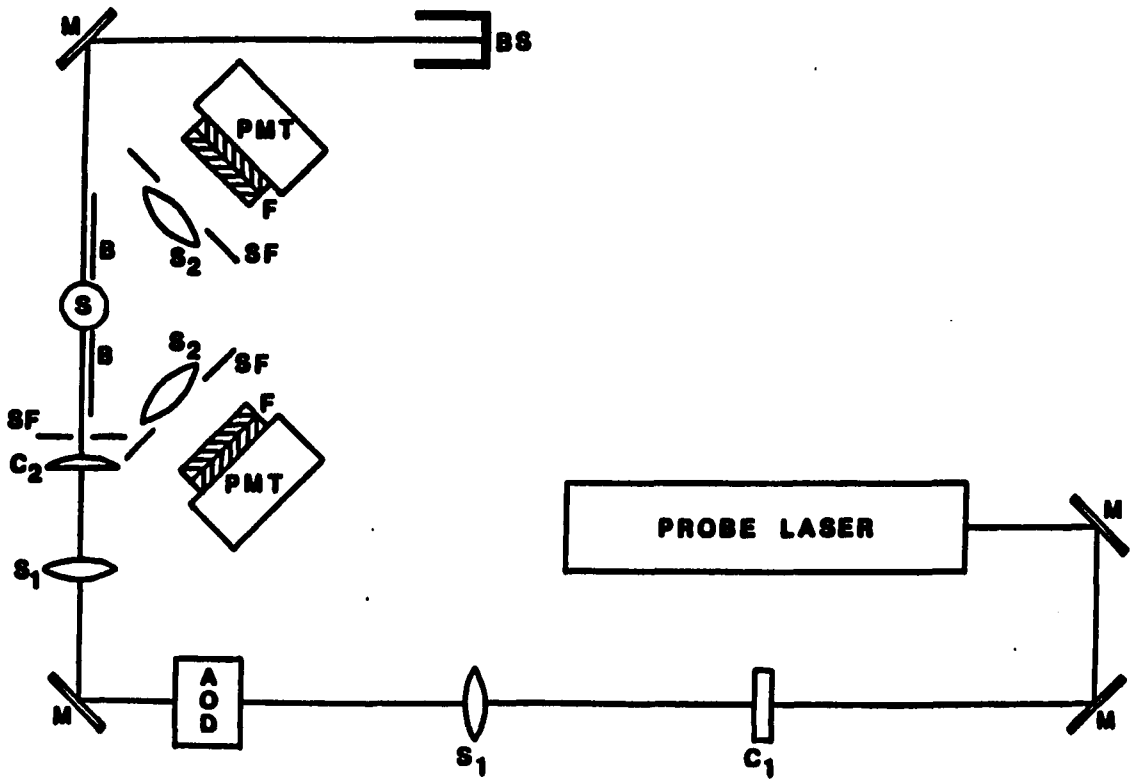

Figure 1. Experimental arrangement for the determination of dissymmetry ratios in laser generated plumes: PROBE LASER, argon ion laser (488 nm); M, mirror; C_1, 5 cm f.l. cylindrical lens; S_1, 50 cm f.l. spherical lens; AOD, acousto-optic deflector placed for vertical deflection; C_2, 30 cm f.l. cylindrical lens; SF, spatial filter; S, sample of pyrolytic graphite; BS, beam stop; B, baffles; S_2, 7.5 cm f.l. spherical lens; F, 488 nm line filters; PMT, photomultiplier tube

1:1 imaging. The collection angle was ~10°. Care was taken to center the lenses with respect to the center of the scattering region. Baffles, B, were used to reduce background scatter. The imaged light was filtered using two 488 nm line filters, F, (Corion Corporation, Holliston, MA, P1-488) with a bandpass of 1 nm placed before each detector. Transparent tape was placed on the surface of the detector windows to slightly diffuse the image at the photocathodes. The detector outputs were amplified by passing them through separate oscilloscopes (Tektronix, Beaverton, OR, Models 7904 and 7704A with amplifier Models 7A12 and 7A15) and fed into the data collection system (Data Precision, Danvers, MA, Model 6000/620 with D1000 preamplifier). The signals for single plumes were digitized with 8 bit resolution at 10 MHz. A total of 16 K-bytes of data were collected for each channel, so each plume was followed for ~1.5 ms. The data collection system was triggered relative to the start of the first scan after firing of the vaporization laser. This was done by using two one-shots in series with the SYNCH OUT from the vaporization laser and the waveform generator as inputs. The delay between the vaporization laser pulse and data acquisition is therefore arbitrary, but <20 μs (the period of a single scan of the probe beam). Scattering signals were collected for single plumes and then transferred via an IEEE488 interface (Capital Equipment Corporation, Burlington, MA, PC<>488) to a microcomputer (IBM, Boca Raton, CA, PC/AT) for storage and analysis.

Photomultiplier gains must be matched between the detectors throughout the probed region for an accurate measurement of the dissymmetry ratio. The emission from the plume itself was initially used

to match the response of the detectors, but the match was not accurate at all locations of the plume. This was attributed to the fact that the emission is contained within the first ~2 mm of the plume, but scattering was collected over ~6 mm. This spatial difference is maintained at the photocathodes, which have spatial variations in gain.

A tungsten lamp, which has an element that is helical and straight, was then used to match gains. The lamp emits uniformly over a vertical region of approximately the same length as the scattering region of the plume. The bulb was carefully aligned with the vaporization beam and the probe beam. A single detector was positioned first at one observation angle and then at the other, maximizing its output signal at each with a constant applied high voltage. This fixes the positions required for collection efficiencies at both angles. The first detector was left at one of the positions and the second detector was then placed at the other position. The gains were then matched by adjusting the voltages applied to the individual detectors. The match was checked at different bulb intensities and was found to be better than 10% over the range used for detection.

The vaporization laser was the fundamental output, 1064 nm, of a Nd:YAG laser (Quantel, Santa Clara, CA, Model VG480) operated at 2.5 Hz with a 10 ns pulse. Typical energy at the sample was 150 μJ/pulse. The lower energy pulses were produced by using reflections off glass slides. The beam was directed perpendicular to the sample surface and focused with a 10 cm focal length spherical lens to a spot size of ~0.2 mm diameter.

The sample was pyrolytic graphite (Union Carbide Corporation,

Cleveland, OH). The surface was finished with 600 grit sandpaper. A piece of transparent tape was used to remove the top layer of graphite and powder residue. Room air circulation was minimized, since the sample was open to the atmosphere.

Mie scattering functions were evaluated using Fortran programs (Microsoft Corporation, Fortran 77 version 4.01) on a microcomputer. Accuracy of the calculations was checked against previously published values. The theoretical dissymmetry ratio for carbon with $m = 1.93-0.656\iota$ at $\lambda = 488$ nm (22) and α up to 10 is shown in Figure 2. The single-valued region extends to $\alpha = 1.1$ ($r = 0.085$ μm, $\iota_1(45°)/\iota_1(135°) = 3.0$). The Rayleigh region ($r < \lambda/20$) begins at $\alpha = 0.31$. The oscillations dampen at larger particle sizes to a ratio of ~3.1. The maximum dissymmetry ratios for the first two peaks are 106.8 and 21.6 at $\alpha = 1.8$ and $\alpha = 2.89$ respectively. The sum of the theoretical scattering signal at 45° and 135° is plotted in Figure 3. This plot provides an idea of the change in scattering efficiency with size.

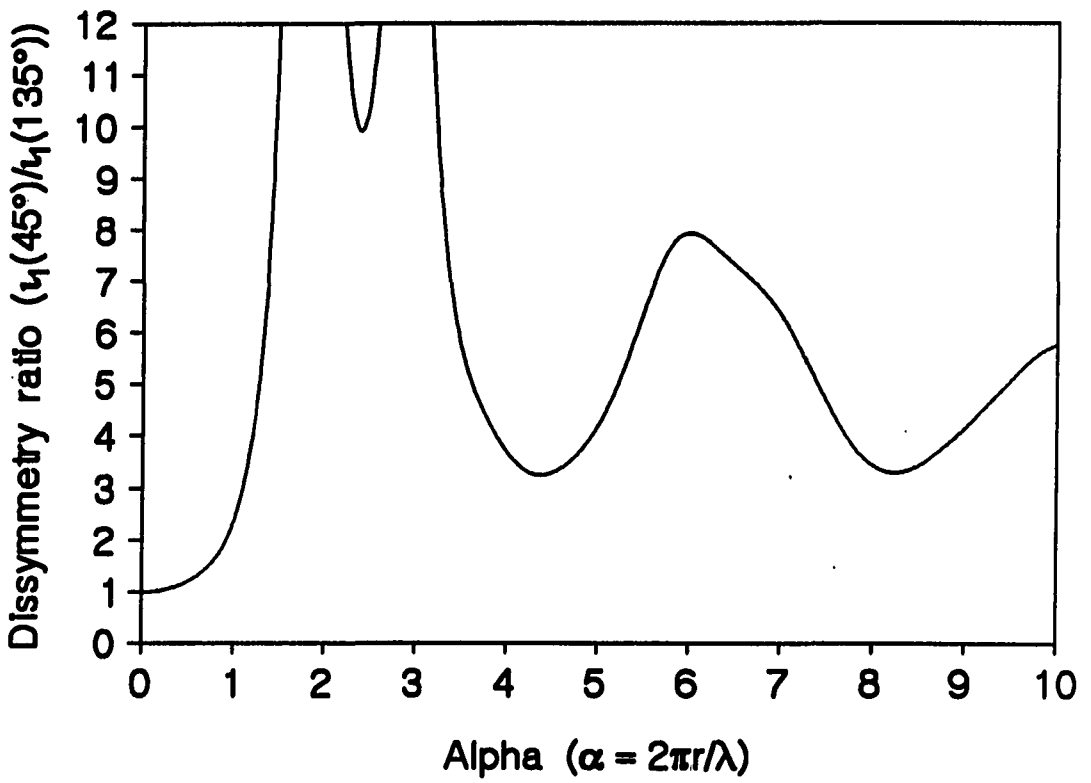

Figure 2. Theoretical dissymmetry ratios of carbon particles based on $m = 1.93 - 0.656i$. The maximum values for the first two peaks are 106.8 and 21.6 at $\alpha = 1.8$ and $\alpha = 2.89$ respectively

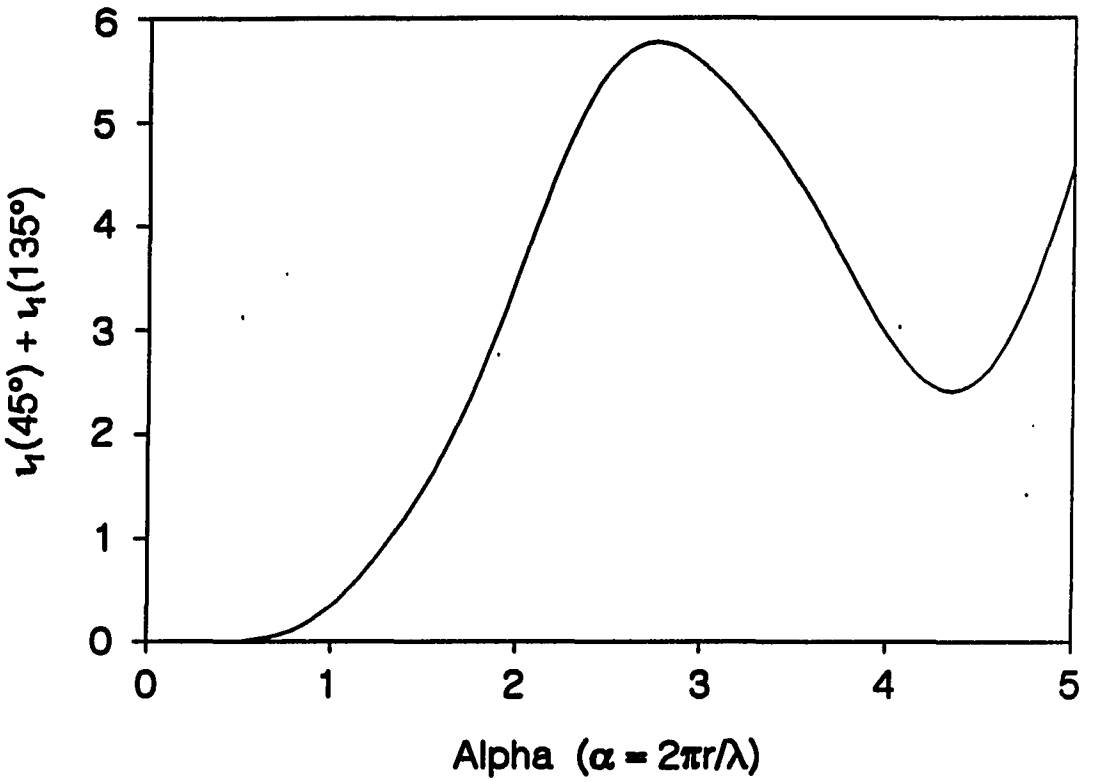

Figure 3. Sum of the theoretical scattering at 45° and 135° for ι_1 based on m = 1.93 - 0.656ι

RESULTS AND DISCUSSION

Figure 4 is a plot of the experimental dissymmetry ratios for pyrolytic graphite. The ratios that lie in the single-valued region, shown as white boxes, span the size range of 0.024 μm to 0.085 μm in radius. The ratios that lie outside of the single-valued region, shown as filled boxes, indicate regions where the average radius is >0.085 μm. Not marked are regions where the intensities are too low or too high to allow the determination of α with confidence.

Since every laser generated plume is different, it is not possible to infer general trends. However, for the specific example shown in Figure 4, several features are evident. To the left of the plot (early in time), there is a distinct region dominated by larger (>0.085 μm) particles. These travel with a high velocity away from the surface. This reflects a violent ejection of material early on that is characteristic of sputtering. Smaller particles (<0.085 μm) over the major portion of the plot have lower velocities and are continuously produced from the surface. The features are consistent with thermal vaporization. In the middle of Figure 4 there is a different group of large particles. These did not originate from the surface and the velocities are similar to the smaller particles that surround this group. It is likely that they are formed by condensation of the smaller particles as they cool and as they collide with each other above the surface.

Figure 5 is a contour map of the total scattering signals at the two angles, adjusted for deflection efficiency of the AOD, for the same plume

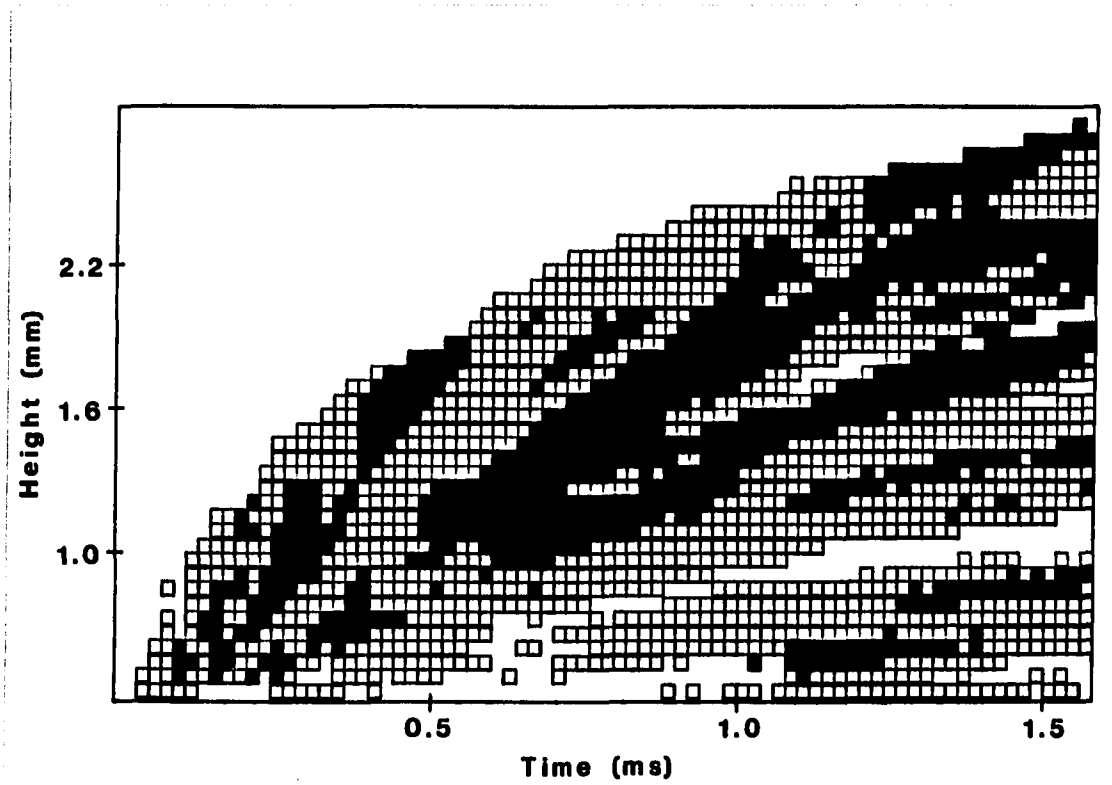

Figure 4. Experimental dissymmetry ratios of carbon particles.
□: ratios in the single-valued region of the theoretical curve ($0.024\ \mu m < r < 0.085\ \mu m$); ■: ratios in the multivalued region of the theoretical curve ($r > 0.085\ \mu m$)

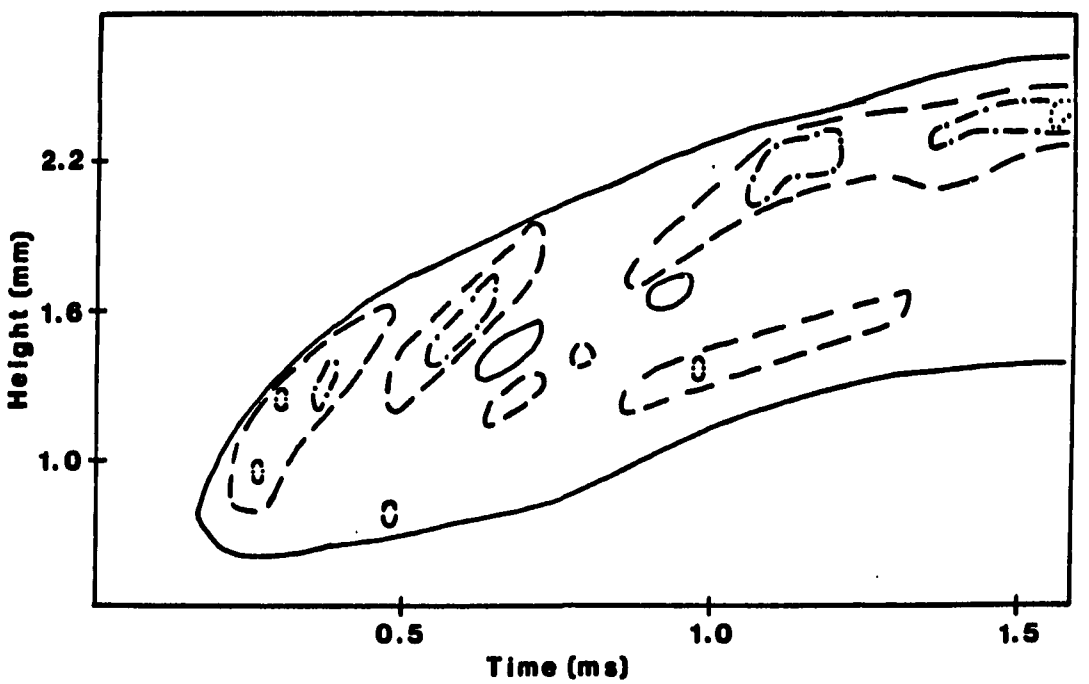

Figure 5. Contour plot of relative total scattering signals ($\iota_1(45°) + \iota_1(135°)$) for the same plume as that shown in Figure 4. Contours are for 1 ——— , 2 — — — , 3 — • — , and 4 • • • •

as that shown in Figure 4. The contours denote relative signal strengths. Dissymmetry ratios as large as 24 are observed in these plumes. Large ratios, >10, were not observed when the laser power density for vaporization is reduced to ~1/2 that used for the plume shown in Figure 4. Ratios >10 have possible sizes limited to those within the first two lobes of the theoretical curve (0.113 μm < r < 0.250 μm). Ratios <10 but >3 span a much larger region of the theoretical curve (r < 0.113 μm or r > 0.250 μm). According to the number density distribution observed by Arrowsmith and Hughes (15), we would expect particles of ~0.250 μm to have a much lower number density, less than 1%, than particles of 0.113 μm. Yet the scattering efficiency of 0.250 μm particles is only 2.5 times greater than that for 0.113 μm particles. So, the scattering efficiency cannot compensate for the expected reduction in the number density of large (r > 0.250 μm) particles. Total scattering intensity in Figure 5 does not show a size relationship. We can therefore conclude that all of the data shown in Figure 4 are on the first lobe of the theoretical curve, and a particle size can be assigned to each pixel. The sizes were found to vary greatly as a function of height and time, so no contour plot based on size is constructed from these results.

Among the many assumptions in the scattering theory is the one of homogeneous size. When instead a size distribution is taken into account in the calculations of the scattering functions, the oscillations in the theoretical curve will broaden and dampen. We must recognize that any size derived from this type of experiment is an average that is weighted more heavily towards larger sizes. The effect is an overestimate of the

size, possibly by up to a factor of two (23).

The assumption of sphericity has been shown to be less important for systems where particle orientation in space is random due to tumbling and where there exists a broad distribution function (23). We would expect both of these factors to be true in these laser generated plumes due to the violent nature of the vaporization process and the high temperatures expected.

The accuracy of refractive index values is a major stumbling block in light scattering methods for particle size analysis. The refractive index used in this study is not the limiting factor for accuracy, since there are other sources of error that contribute more significantly, such as the match between the detectors and the assumption of homogeneous size in the theoretical calculations.

In conclusion, a new method for particle size analysis in laser generated plumes with good temporal and spatial resolution has been demonstrated. The analysis is done in situ. Using multiple scattering techniques for a single plume, such as combining polarization (14) and dissymmetry ratios, would provide even greater accuracy in the size determination. Multiple measurements would also extend the region of sizeable particles. Large particles from laser microprobe systems have been observed by others (13-15, 24). Rohlfing calculated a rough estimate of the size of carbon particles generated from a graphite rod using the second harmonic, 532 nm, of a Q-switched Nd:YAG laser for ablation at ~3 $X10^8$ W/cm^2. He calculated an average size of ~0.06-0.11 μm in radius. In fact, laser vaporization has been used specifically as a

particle generator (25) to make ~10 nm sized particles. The fact that such large particles can be generated in these plumes could be of particular interest to researchers involved in studies of large clusters formed from laser ablation.

REFERENCES

1. Laqua, K. In Analytical Laser Spectroscopy; Omenetto, N., Ed.; Wiley: New York, 1979; Chapter 2.

2. Ready, J. F. Effects of High-Power Laser Radiation; Academic: New York, 1971.

3. Piepmeier, E. H. In Analytical Application of Lasers; Piepmeier, E. H., Ed.; Wiley: New York, 1986; Chapter 19.

4. Conzemius, R. J.; Capellen, J. M. Int. J. Mass Spectrom. Ion Phys. 1980, 34, 197-271.

5. Dittrich, K.; Wennrich, R. Prog. Anal. Atom. Spectrosc. 1984, 7, 139-198.

6. Arrowsmith, P. Anal. Chem. 1987, 59, 1437.

7. Wennrich, R.; Dittrich, K. Spectrochim. Acta 1982, 37B, 913-919.

8. Talmi, Y.; Sieper, H. P.; Moenke-Blankenburg, L. Anal. Chim. Acta 1981, 127, 71-85.

9. Chen, G.; Yeung, E. S. Anal. Chem. 1988, 60, 864.

10. Chen, G.; Yeung, E. S. Anal. Chem. 1988, 60, 2258.

11. Huie, C. W.; Yeung, E. S. Appl. Spectrosc. 1986, 40, 863.

12. Yappert, M. C.; Kimbrell, S. M.; Yeung, E. S. Appl. Opt. 1987, 26, 3536.

13. Huie, C. W.; Yeung, E. S. Anal. Chem. 1986, 58, 1989.

14. Kimbrell, S. M.; Yeung, E. S. Spectrochim. Acta 1988, 43B, 529.

15. Arrowsmith, P.; Hughes, S. K. Appl. Spectrosc. 1988, 42, 1231.

16. Mie, G. Ann. Physik 1908, 25, 377.

17. Meehan, E. J.; Beattie, W. H. J. Phys. Chem. 1960, 64, 1006.

18. Sinclair, D.; La Mer, V. K. Chem. Rev. 1949, 44, 245.

19. van de Hulst, H. C. Light Scattering By Small Particles; Dover: New York, 1981.

20. Kerker, M. The Scattering of Light and Other Electromagnetic Radiation; Academic Press: New York, 1969.

21. Lowan, A. N. Tables of Scattering Functions for Spherical Particles; National Bureau of Standards: Washington, D.C., 1948; A.M.S.-4.

22. Leib, K. G. Determination of the Attenuation of Laser Beams by Clouds of Particulate Matter; NTIS AD-756205, 1973.

23. Bonczyk, P. A. Combust. Flame 1979, 35, 191.

24. Rohlfing, E. A. J. Chem. Phys. 1988, 89, 6103.

25. Araya, T.; Matsunawa, A.; Katayama, S.; Hioki, S.; Ibaraki, Y; Endo, Y. U.S. Patent 4,619,691, 1986.

SECTION III

SPATIAL AND TEMPORAL DISTRIBUTIONS OF LARGE MOLECULES IN PLUMES GENERATED BY LASER DESORPTION

INTRODUCTION

Lasers have been used since 1962 to vaporize small amounts of solid inorganic material (1). More recently their use to vaporize (desorb) large thermally labile organic molecules has grown. The larger and more polar the molecule, the more difficult it is to volatilize it by traditional means without thermal degradation. The advantage of using a laser to generate gas phase species, as opposed to the traditional thermal means, is that the laser induces a rapid temperature increase, up to 10^{11} K/s (2), which can allow desorption to be favored over decomposition (3, 4). Analytical measurements can then be performed on large molecules in the gas phase.

The ultraviolet-visible absorption spectra of tyrosine, Dopa, dopamine, adenine, and norepinephrine in the gas phase after laser desorption have been demonstrated (5). Laser desorption (LD) from thin layer chromatography (TLC) plates has been coupled with gas chromatographic separation (6) with electron capture detection and with supersonic jet fluorometric detection (7). By far, the most common detection method uses mass spectrometry (MS) (8) which offers excellent sensitivity and suitability for isotopic analysis. Mass spectrometry of surface-bound species has in the past relied on fast atom bombardment (FAB), field desorption (FD), and secondary ion MS (SIMS) to generate gas phase ions of large molecules. The advantages of LD over these include the ability to perform high-resolution spatial analysis, suitability for non-conducting surfaces, lack of high vacuum requirements, and greater

control over the extent of fragmentation through the judicious choice of power density and wavelength. LD with MS detection is typically operated in one of two modes. The first and more common mode is laser induced ionization (4). Vaporization and ionization occur at the same step, though the modes of ionization are not clear (9, 10). The second mode of operation separates desorption from the ionization step. Lower power densities or lower photon energies are used to promote desorption of neutrals. Then, ionization is performed using nonselective ionization such as electron beam (11), multiphoton ionization (12), and chemical ionization (13), or a more selective mode of ionization such as resonance two photon ionization (14). Molecules at least as large as 250000 g/mole have been detected using matrix assisted laser desorption with mass spectrometric detection (15). Even DNA fragments of at least up to 622 base pairs (~410.5 Kg/mole) are amenable to volatilization by lasers (16).

The vaporization laser in the desorption mode imparts its energy to the sample, the substrate, or the sample matrix through absorption. The resulting rapid rise in temperature promotes desorption over degradation. Fragmentation is thought to arise from (8):

1. Direct action from the laser through absorption of enough photons and acquisition of enough internal energy to break bonds.

2. Thermal degradation near the surface, which is supported by the observation of cationized fragments.

3. Decomposition of an unstable parent molecule or ion in the gas phase at some distance from the surface.

The desorption, degradation, and ionization processes and their dependence on laser and sample parameters are not well understood. Brand and George (17) have modelled the effects of laser pulse characteristics and thermal desorption parameters for laser induced thermal desorption. For LD with nanosecond pulses in the ultraviolet region, the influence of vaporization wavelength with respect to strong and weak classical absorption by the analyte molecule has been studied using MS detection (18, 19). Those authors reported that the presence of absorption by the analyte was found to lower the threshold irradiance needed for the detection of parent ions and to increase the ratio of molecular-to-fragment ions.

Most detection schemes for LD are performed external to the developing plume. This paper reports the use of an optical imaging system, based on acousto-optic laser beam deflection (20, 21), to record real time spatial and temporal maps of the desorption of large organic molecules in situ. In contrast to MS methods, the neutral gas phase molecules are probed directly by absorption. The direct observation of the desorbing molecules should provide insight into the desorption process and its dependence on laser and sample parameters.

EXPERIMENTAL

Figure 1 shows the optical set-up for two-dimensional mapping of organic dyes in laser generated plumes by molecular absorption. The argon ion laser, (Laser Ionics, Orlando, FL, Model 554A) was used to probe the desorbed dyes. The 60° prism, P, dispersed the output lines of the argon laser and the 488 nm line was isolated at the aperture of the first acousto-optic deflector (AOD). The beam was ~3 mm when it entered the first AOD (Intra Action, Bellwood, IL, Model ADM-150 and DE-150) which scanned the beam in the vertical direction. The deflected first order beam and part of the zeroth order beam entered the second deflector (Isomet, Springfield, VA, Model 1205-C) which scanned the vertically deflected input beam in the horizontal direction. A 1 m focal length spherical lens, S_1, was positioned next to the second deflector to focus the scanning beam into the plume which is placed at the focal plane of the lens. The aperture, A, blocked any orders other than the (1,1) beam. The other features of the optical set up are the same as that used in Reference 21. A thorough discussion of the operation of AOD as laser beam scanners was given in References 20 and 21.

Asymmetric waveforms of 200 kHz and 10 kHz from two waveform generators (Wavetek Corporation, San Diego, Ca, Models 162 and 182A) were used to control the rf generators for the vertical and horizontal deflector drivers respectively. Thus each scan was unidirectional with periods of 5 μs and 100 μs and reset times of ~0.25 μs and ~5 μs for the vertical and horizontal scans respectively. Synchronization was achieved

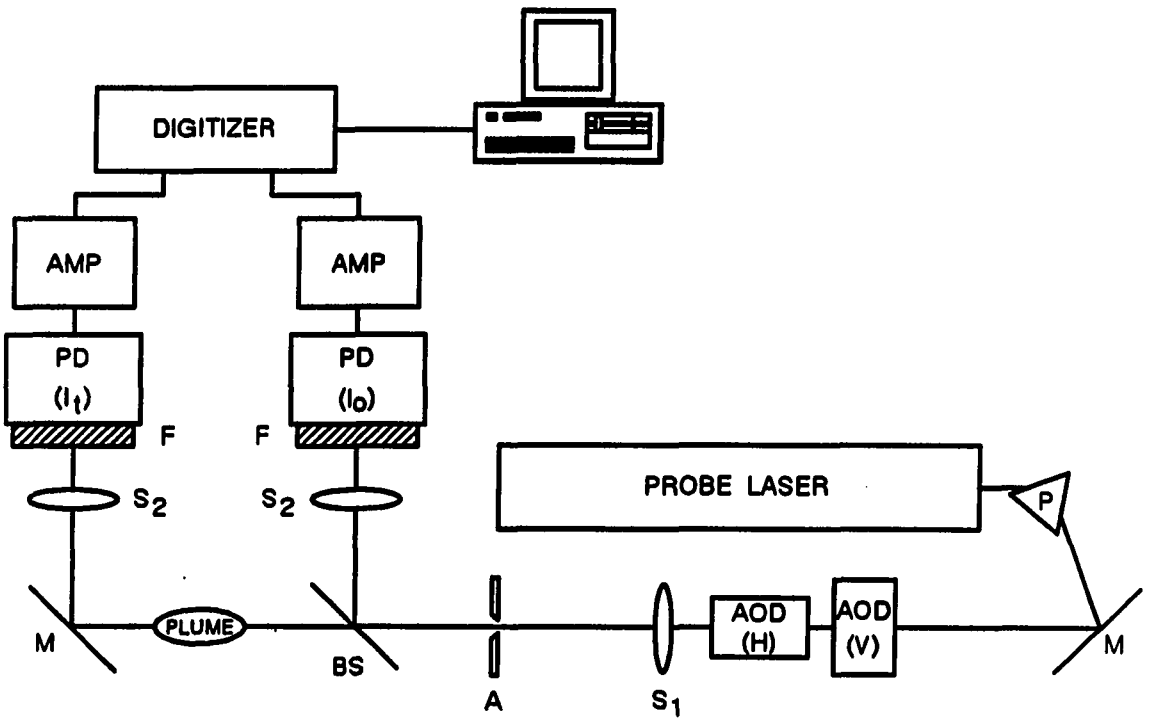

Figure 1. Experimental arrangement for two-dimensional imaging of laser-desorbed organic dyes by absorption: PROBE LASER, Argon ion laser; P, 60° prism; M, mirror; AOD, acousto-optic deflector; S_1, 100 cm f.l. spherical lens; A, aperture; BS, 50% beamsplitter; S_2, 7.5 cm f.l. spherical lens; F, 488 nm line filter; PD, photodiode; AMP, amplifier

between the horizontal and vertical scans by triggering the slow waveform (10 kHz) with the SYNCH OUT from the fast waveform generator (200 kHz).

When acousto-optic deflectors are operated at fast scan times, the refractive index grating induced in the acoustic medium can have a significant cylindrical lens effect in the direction of the scan (22). Because the scan time for the vertical deflection was short, the induced cylindrical lens in the vertical deflector was significant (~1.7 m) when compared to the focal length (1 m) of the lens used to focus the scanning beam. But, the induced cylindrical lens in the horizontal deflector (~34.5 m) was not significant. So, the optimum focus for the two dimensions was not at the same location and a compromise in resolution for one of the dimensions, horizontal in this case, had to made. Ideally, when this effect is significant in a two dimensional scanning operation, focusing in the two dimensions should be done with cylindrical lenses so as to obtain optimum resolution in both directions. Due to the lack of long focal length cylindrical optics (which are desirable to achieve the scan length needed to map the plume), the spherical lens was used instead and resolution was compromised. For the experiments, conducted here, resolution of 40 X 12 spots in an 8 X 5 mm scan was confirmed by placing a grid at the focus of the image and measuring transmittance with a photodiode.

To take into account any changes in laser intensity, as well as efficiency differences in the deflectors as the beam is scanned, a 50% beam splitter, BS, was placed before the sample cell to reflect half of the probe beam to a second detector. The reflected beam was focused onto

a photodiode (Hamamatsu, Middlesex, NJ, Model S1790-01) to monitor the incident intensity. The sample beam probed the plume and the transmitted part was focused onto another photodiode. Line filters, F, with 1 nm bandpasses at 488 nm (Corion Corp., Holliston, MA, Model P1-488) were used before the photodiodes to reduce background radiation.

Both sample and reference signals were amplified by passing them through separate oscilloscopes (Tektronix, Beaverton, OR, Models 7904 and 7704A with 7A15 and 7A16 amplifiers) and fed into the data acquisition system (Data Precision, Danvers, MA, Model 6000/620 with D1000 preamplifier). The digitizer was operated at 10 MHz, with 8 bit resolution. A total of 16 K-bytes was collected in each channel for a single vaporization event. Thus, the molecular population was monitored for 1.6 ms. In this way, up to sixteen two-dimensional images were collected for single plumes. The acquired data were transferred to a microcomputer (IBM) through an IEEE488 interface (Capital Equipment) where they were evaluated. Data acquisition was triggered by the SYNCH OUT from the vaporization laser which occurs ~160 ns prior to lasing.

The first step in data processing was the subtraction of background signals and standardization of the signals to take into account any differences (except sample absorption) along the optical paths of the two beams and any differences in the degrees of amplification in the electronics. The two-dimensional standardization files were calculated from an average ratio (sample to reference) of 16 consecutive two dimensional scans in the absence of desorption. The relative standard deviations did not exceed 3% except at the extremes of the horizontal

scans where deflection efficiency changes rapidly. The absorbance was then calculated for each spot and plotted.

The vaporization laser was the frequency doubled, 532 nm, output of a Q-switched Nd:YAG laser (Quantel, Santa Clara, CA, Model VG480) operated at 2.5 Hz, with 10 ns pulse width. Typical energy at the sample surface was 3.5-34 mJ. Power was varied by changing the high voltage at the laser. A reflection off a glass slide was used to monitor energy for each pulse at an energy ratiometer with an energy probe (Laser Precision, Utica, NY, Models Rj-7200 and Rjp734). The vaporization beam was focused to a line by the combination of two cylindrical lenses. A 2.5 cm focal length lens was used to expand the beam lengthwise, parallel to the probe beam, creating the long pathlength. A 10 cm focal length lens, was placed orthogonal to the 2.5 cm focal length lens to focus the beam horizontally. The vaporization laser was focused to a line instead of a spot to provide a longer pathlength over which absorption could occur. This also eliminates the need for deconvoluting a cylindrically symmetric plume. Burn marks on photographic film and on the samples show even burns at high power but not so even at lower power. Uneven vaporization at low power is expected because decreasing the operating voltage of the pulsed laser affects the mode structure of the output beam; it becomes less Gaussian.

The samples consisted of assorted organic dyes dissolved in methanol with 0.1% nitrocellulose (Polyscience, Warrington, PA). The dyes were chosen for their varied absorptivities at 532 nm, the vaporization wavelength. The dyes were rhodamine 6G (Exciton Chemical Co., Dayton, OH), neutral red (Hartman-Leddon Co., Philadelphia, PA), and disodium

fluorescein (Kodak, Rochester, NY). The absorption spectra of the dyes in methanol with 0.1% nitrocellulose matrix are shown in Figure 2. The absorbance by fluorescein is greatly reduced in the matrix due to pH effects. The molar absorbance of fluorescein at 488 nm decreased by a factor of 21 from that for no matrix. The molar absorbance at 488 nm of neutral red increased by ~18% in the matrix, while the molar absorbance of rhodamine 6G decreased by ~8% in the matrix. The dye solutions were prepared with no purification of the compounds.

Solid films of the dyes were made by casting 100 μL of the solution onto 22 X 30 mm glass slides. The solvent was allowed to evaporate at room temperature with room air currents minimized. The method produced fairly uniform films. The nitrocellulose was used to improve film uniformity. This method was evaluated with others for producing reproducible samples for laser ablation with MS detection (23). There, 5% nitrocellulose was used, but at the power densities used here, films cast from 5% solutions would not desorb completely. Complete desorption was desired so total desorbed mass could be calculated. The slides were placed on a mount in an aluminum cell for front illumination. The vaporization beam impinged on the surface of the dye film, and any transmitted light passed the slide and was blocked and scattered by the cell bottom ~2 cm from the slide. Unlike most LD methods which rely on absorption of the laser energy by the substrate or by an added matrix, this arrangement will allow a direct evaluation of the influence of the absorptivity of the sample at the vaporization wavelength on fragmentation and desorption since the substrate is not expected to appreciably absorb

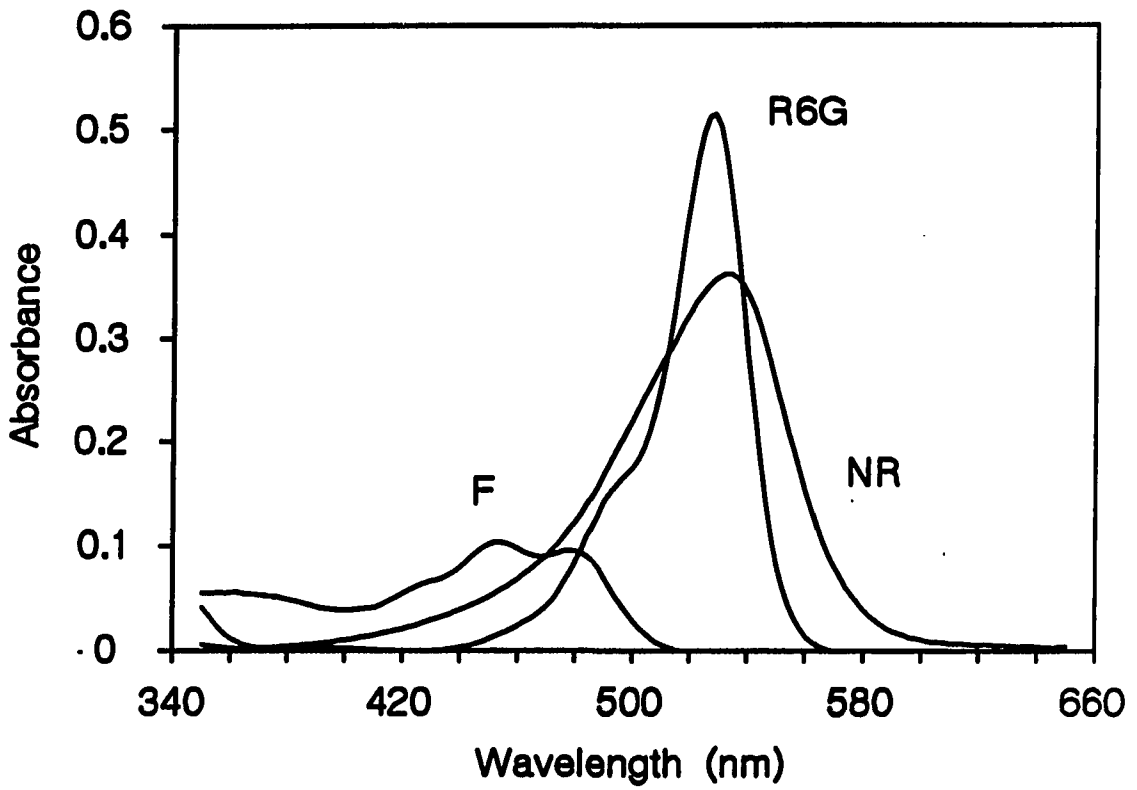

Figure 2. Absorption spectra of organic dyes (1 cm path) in methanol with a 0.1% nitrocellulose matrix: R6G, rhodamine 6G at 5 μM; NR, neutral red at 10.0 μM; F, fluorescein at 66 μM

the laser energy.

The cell has been described previously (24). It has entrance windows for the probe and vaporization beams and exit windows for the probe beam and for observing scatter or fluorescence at 90°. The cell is equipped with a valve for controlling the gaseous environment. All plumes were recorded at 1 atm argon. The cell was pumped out by a mechanical pump and refilled with argon between plumes.

RESULTS AND DISCUSSION

Figure 3 shows pictures of the films made from the three dyes. The pictures from top to bottom are for rhodamine 6G (R6G) made from a 2.8 mM solution, neutral red (NR) made from a 3.5 mM solution, and fluorescein (F) made from a 3.0 mM solution. The black markings are labels from the glass side of the sample. The clear lines in the center of the images are where the vaporization laser desorbed the dye film at two power densities for at least two trials each. The areas vaporized were ~2.2 X 0.033 cm and ~1.5 X 0.02 cm with power densities of ~45 MW/cm^2 and ~13 MW/cm^2 respectively. One can immediately see that more dye was removed at the higher power density. This is due to the changing mode structure of the vaporization laser, providing a larger area with sufficient power density to desorb the dye. Relatively clean vaporization occurs at the higher power densities, leaving few crystallites behind, for R6G and NR. Fluorescein does not appreciably absorb at 532 nm, which accounts for the significant amount of unvaporized material left on the slide made from the fluorescein solution. Fluorescein also gave much lower absorption signals. Close examination of vaporization marks at the lower power density reveals some dye remaining in the center of the line and a less clean edge. This is attributed to the change in mode structure of the vaporization laser as a function of operating voltage. Power is not distributed as uniformly at the lower operating voltage. The estimated masses of R6G and NR desorbed, based on relative areas of the film and the vaporization lines, are 1.5 μg (R6G), 0.61 μg (R6G), 1.1 μg (NR), and

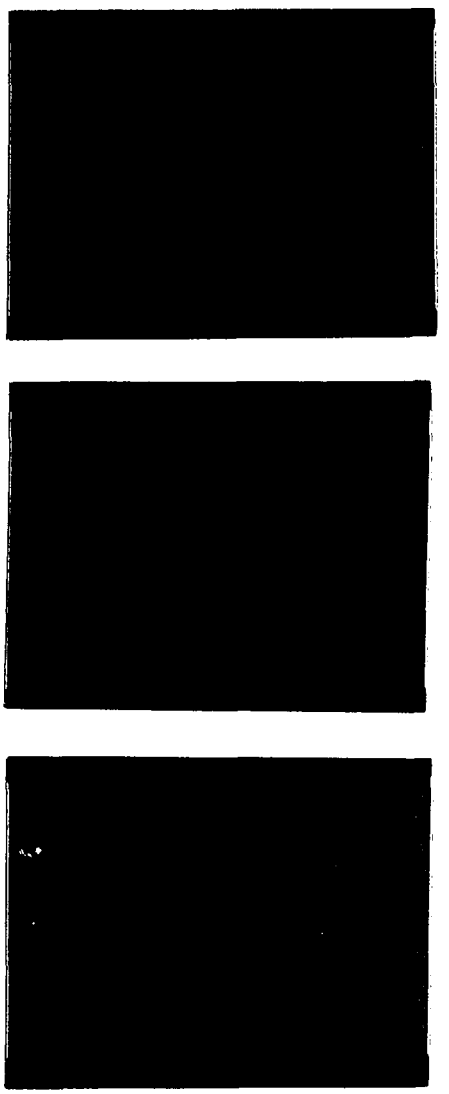

Figure 3. Prints of dye films cast from methanol in a 0.1% nitrocellulose matrix. The top print is rhodamine 6G from a 2.8 mM solution. The middle print is neutral red from a 3.5 mM solution (originally mislabeled). The bottom print is fluorescein from a 3.0 mM solution

0.46 μg (NR) for the high and low power densities respectively.

Figures 4 and 5 show the 2-D absorption profiles for desorption of R6G at low and high power respectively from the film shown in Figure 3. The image shows five consecutive 2-D passes through the plume. The horizontal axis, in the forward part of the graph, reflects the horizontal scan in the plume. The unit numbers on the axis note the beginning of each consecutive horizontal sweep through the plume, which occur at ~100 μs intervals. The other horizontal axis shows the probe height above the sample surface. At the beginning of some of the 2-D images, one can see a signal in the first vertical scan. This signal is a result of the reset in the horizontal scanner. When the laser beam reaches the end of the 2-D scan, it is quickly swept back to the beginning of the 2-D sweep. As the beam re-traverses the plume, it produces another record of the absorption. One immediately notices that at lower power density, there is more absorption, even though less dye was actually vaporized. This is a clear indication of destruction of the chromophore with increasing power density. Increased fragmentation with increasing power density has been noted before when using MS detection (25).

Figures 6 and 7 show similar plots at low and high power for the neutral red film shown in Figure 3. Figure 7 is an extended series of plots showing the rest of the acquired images of the NR plume at high power. Again, the lower power plot shows greater absorption, when normalized for the amount of material desorbed, indicating destruction of the chromophore. But destruction does not occur to the same extent as for R6G. NR has lower absorptivities at 532 nm and at 488 nm than R6G, but

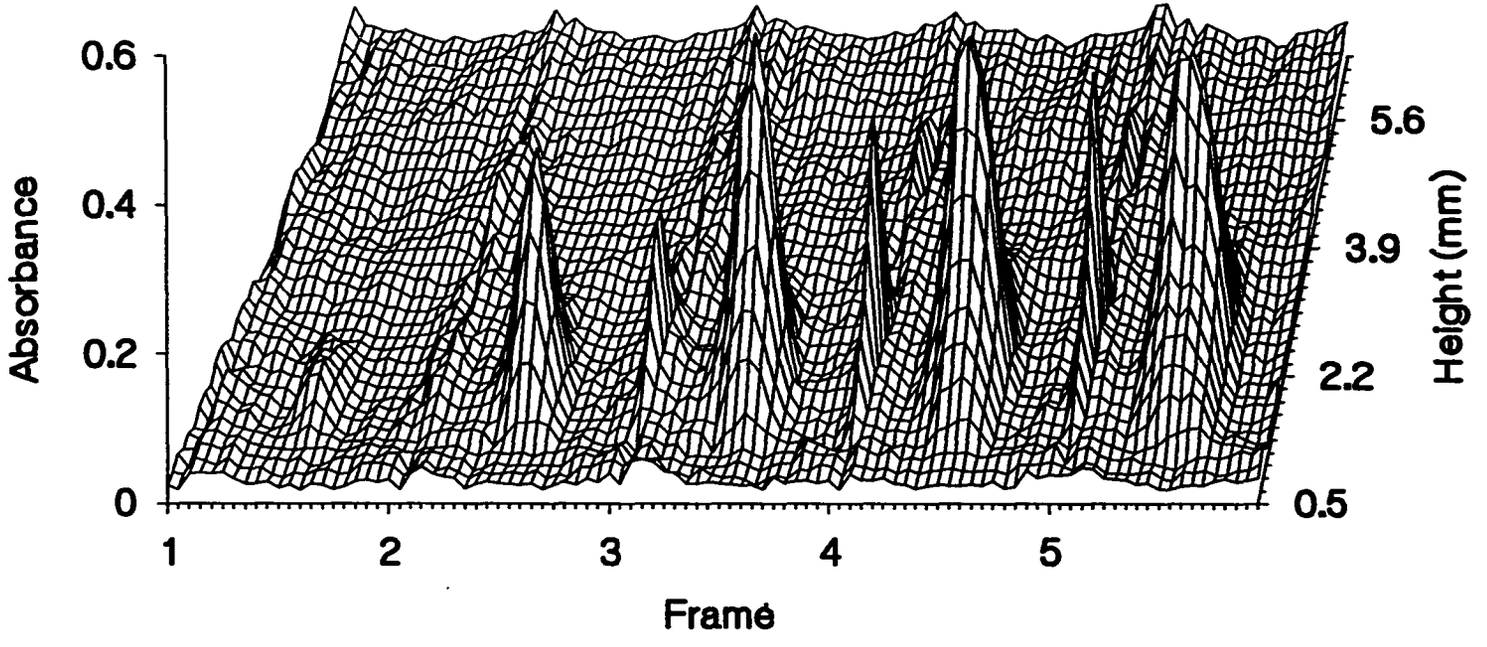

Figure 4. Consecutive 2-D plots of absorption by R6G in a laser-generated plume for 0.61 μg desorbed dye at 13 MW/cm^2, 1.5 cm absorption path

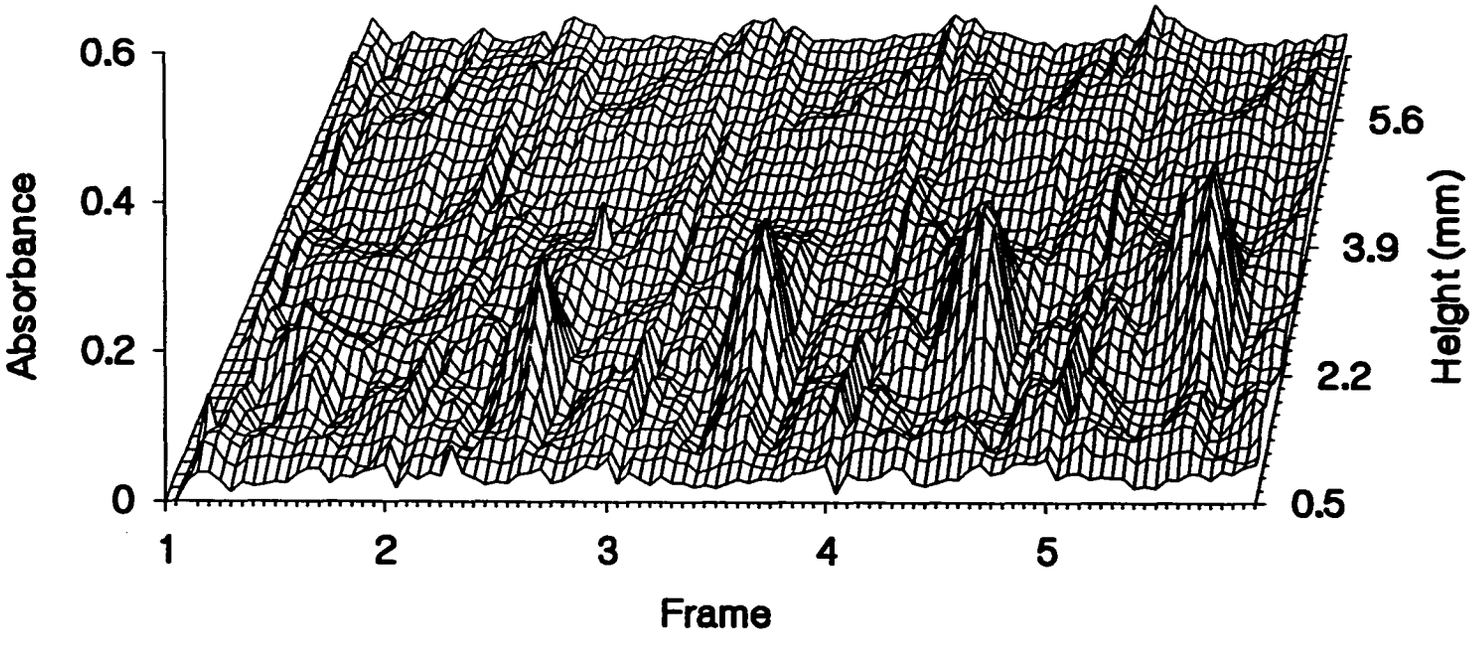

Figure 5. Consecutive 2-D plots of absorption by R6G in a laser-generated plume for 1.5 μg desorbed dye at 47 MW/cm^2, 2.2 cm absorption path

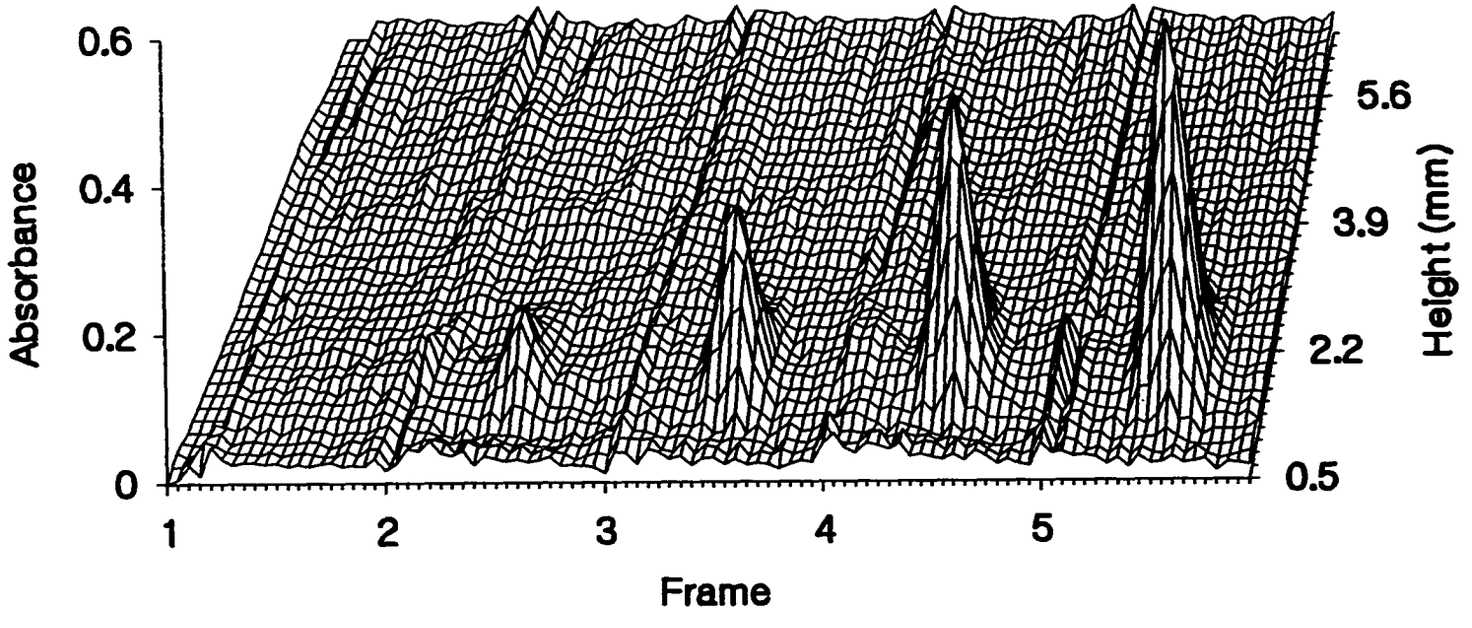

Figure 6. Consecutive 2-D plots of absorption by NR in a laser-generated plume for 0.46 μg desorbed dye at 13 MW/cm^2, 1.5 cm absorption path

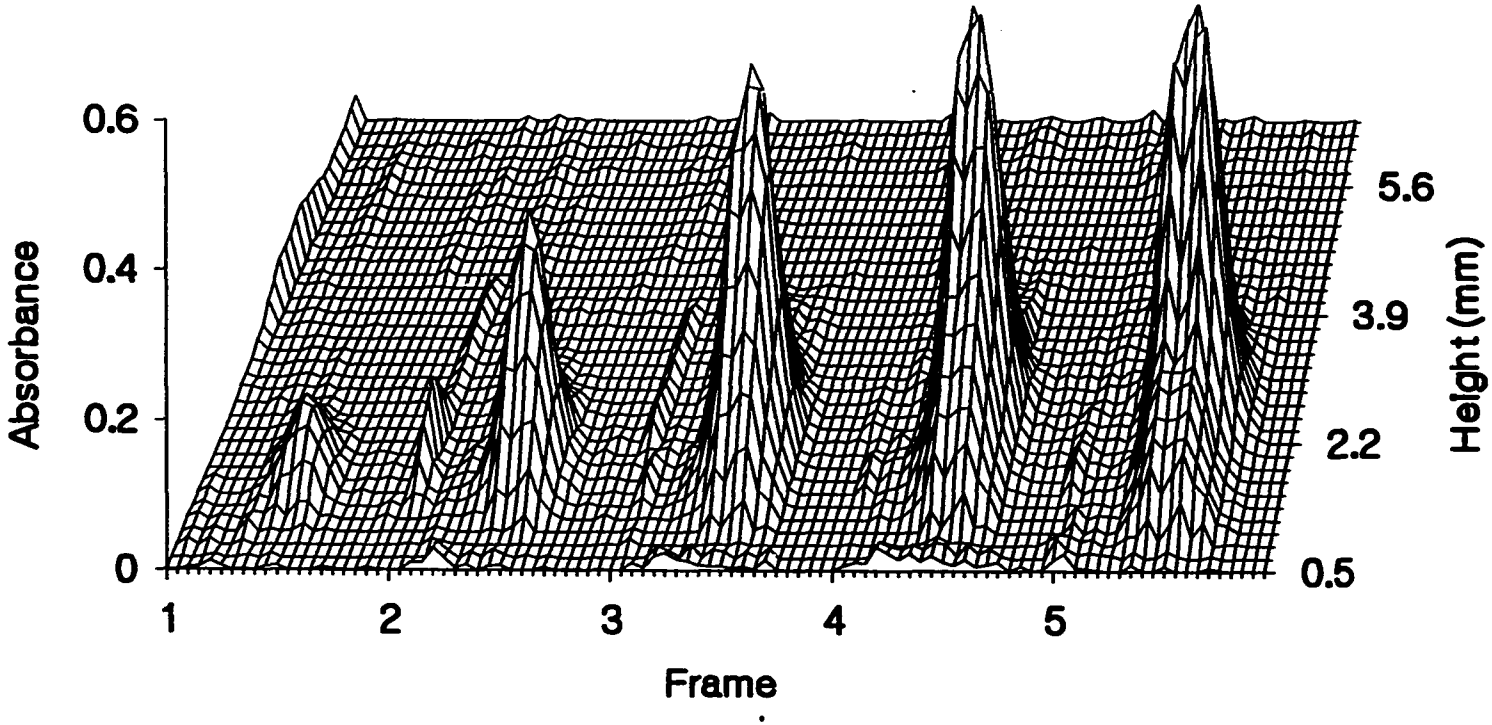

Figure 7a. Consecutive 2-D plots of absorption by NR in a laser-generated plume for 1.1 μg desorbed dye at 44 MW/cm^2, 2.2 cm absorption path

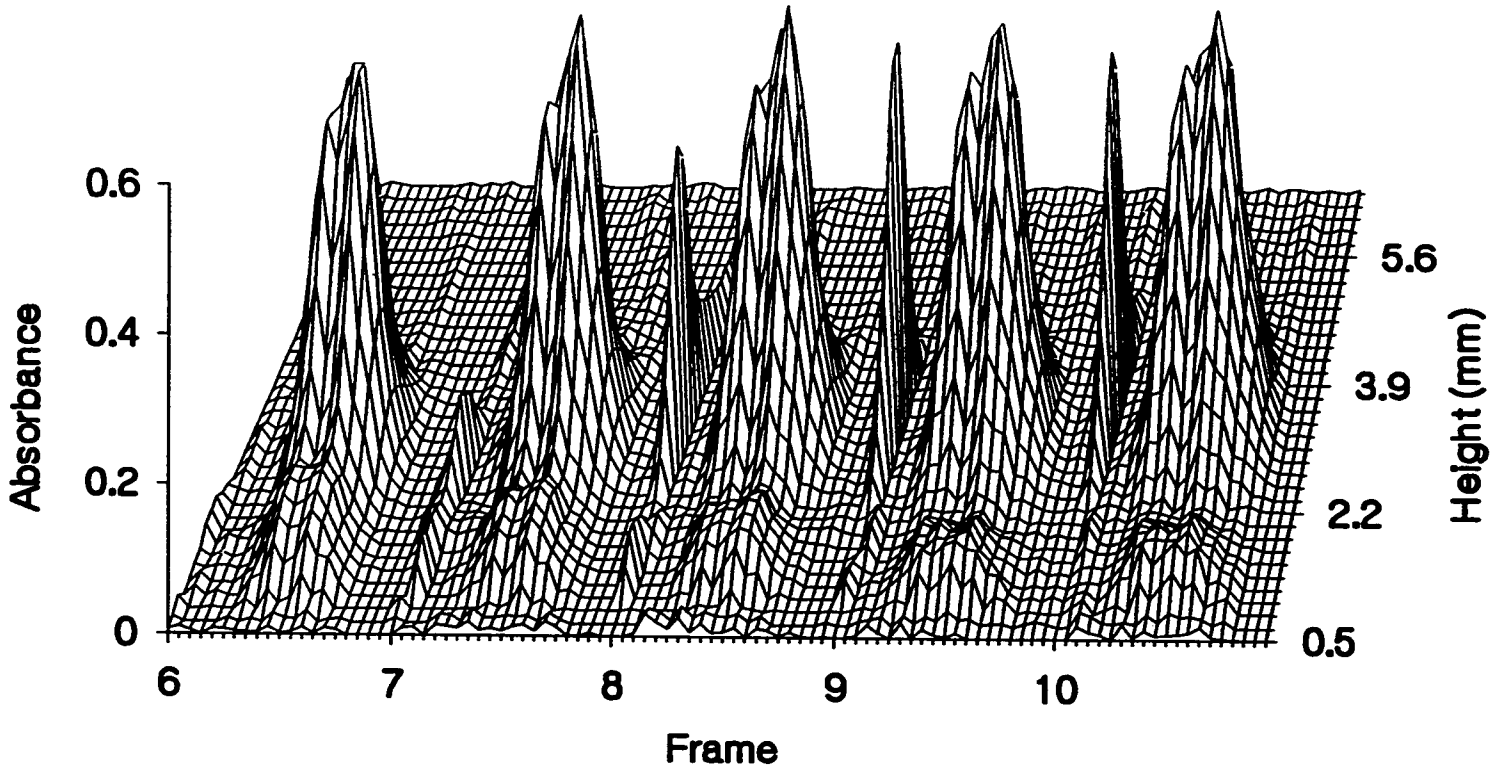

Figure 7b. Continued

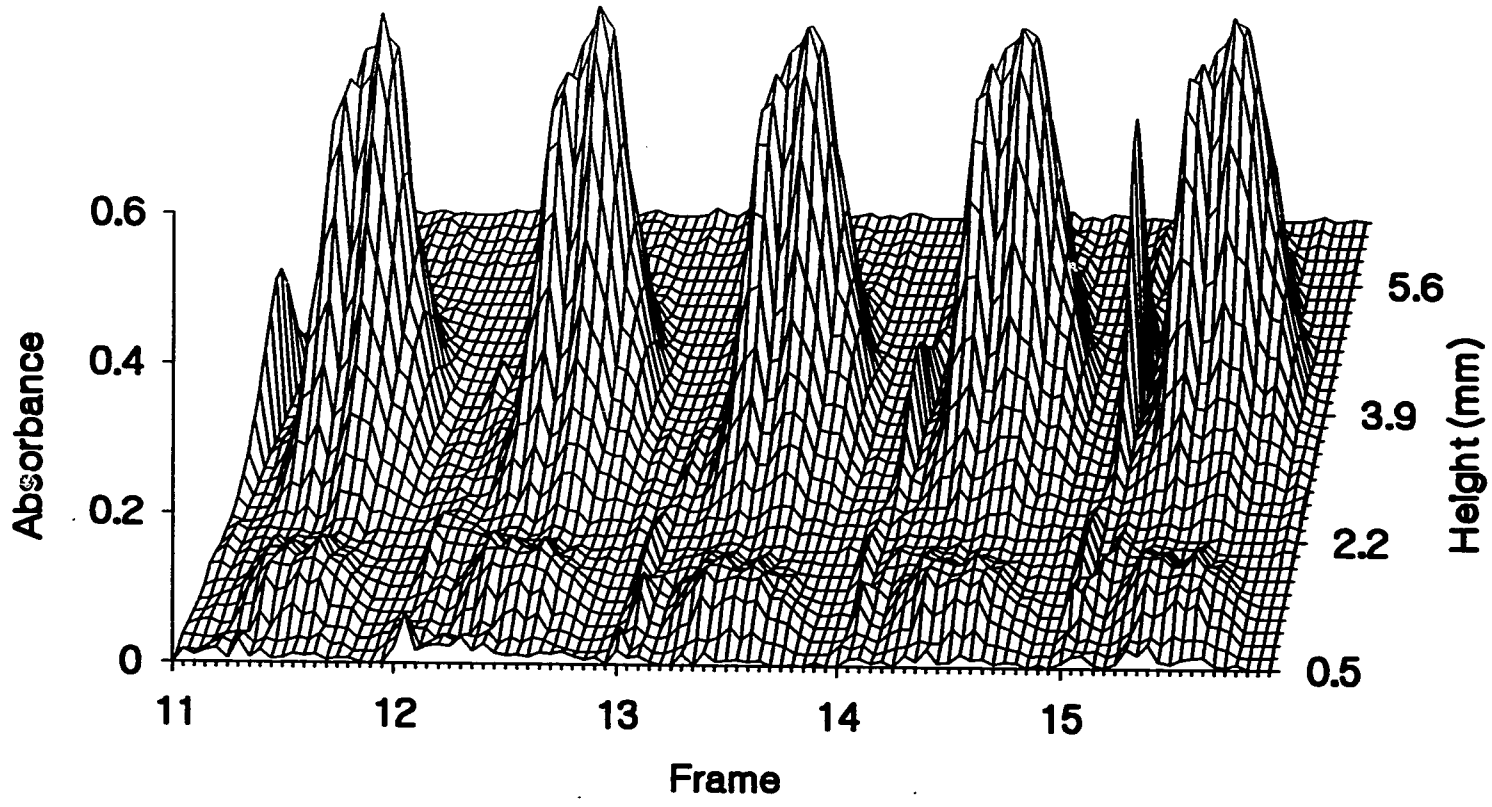

Figure 7c. Continued

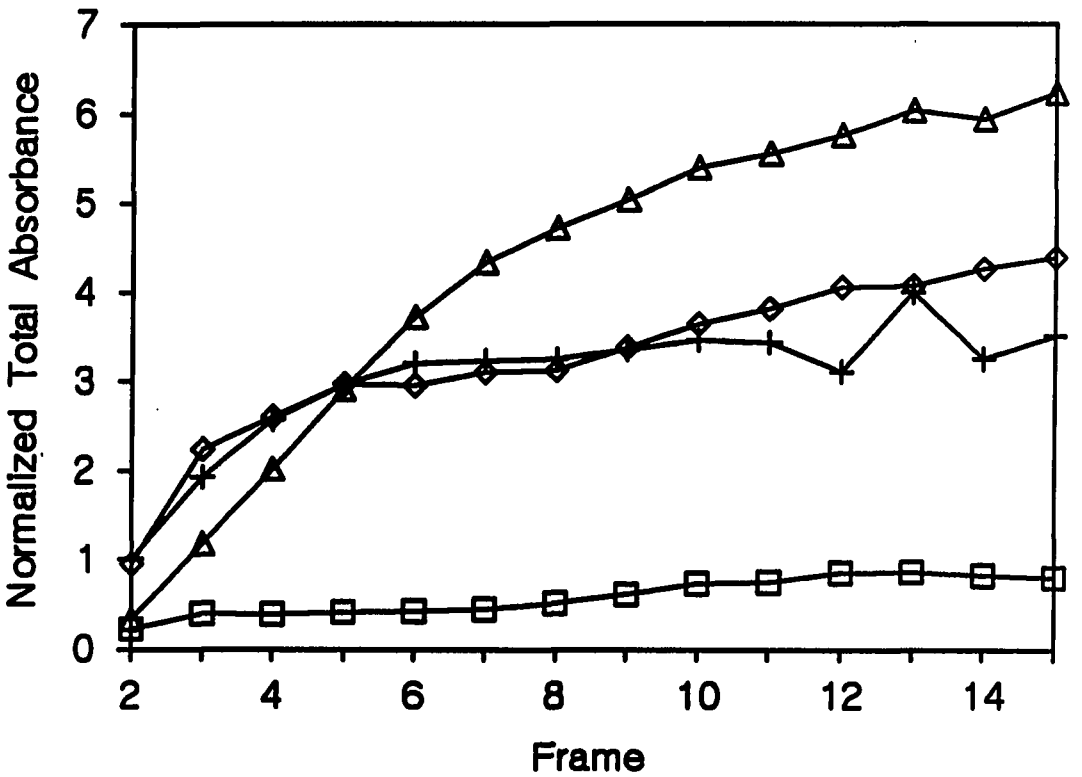

Figure 8. Normalized total absorbance of R6G and NR for the plumes shown in Figures 4-7: +, R6G plume, 13 MW/cm^2; □, R6G plume, 47 MW/cm^2; △, NR plume, 13 MW/cm^2; ◇, NR plume, 44 MW/cm^2

higher peak absorbance were produced in the plume. Figure 8 is a plot of the integrated absorbance in the plumes at each of the frames shown in Figures 4-7 normalized for desorbed mass, absorptivity at 488 nm, and pathlength. Duplicate experiments at each vaporization condition essentially gave the same results as shown here. This depicts the power dependence and the absorptivity dependence (at the vaporization wavelength) of the relative extent of chromophore destruction. The plots show a consistent growth in total absorbance for all conditions, so the dye continues to be desorbed from the surface well after the vaporization laser pulse. This is in contrast to earlier studies (21) of Na atoms ablated from a $Na_{0.7}WO_3$ sample where the peak in atomic absorption was observed in the first ~67 μs of the plume with a gradual decay in signal thereafter. The steady increase in total absorbance here also indicates that the major amount of fragmentation occurs early (<100 μs) in the desorption process and not at some longer time at a distance from the surface.

Figure 7 shows the entire set of the 2-D scans through the neutral red plume at high power density. The desorption process is very gradual, extending well after the vaporization pulse is over. The plume expands and begins to become more diffuse. The residual signal near the surface in the later frames is possibly due to some later desorbing dye. At this pressure, the molecules do not travel far from the surface, and they diffuse slowly in time. At lower power, the dye travels away from the surface and diffuses more slowly. For the plume shown in Figure 7 (NR, high power), the location of the absorption maximum moves away from the

surface at ~3.5 m/s initially (~0.5 ms) but it gradually slows to ~1.6 m/s. The front of the plume travels at ~5.2 m/s for the first ~0.5 ms but also slows quickly to ~1.7 m/s. At lower power for NR, Figure 6, the location of the absorption maximum moves at ~1.7 m/s for ~0.4 ms and slows to ~0.8 m/s. The front travels at ~3.5 m/s for ~0.2 ms, slowing to ~1.3 m/s and later appearing almost stationary. Lateral diffusion velocity is ~1 m/s and ~0.8 m/s for the plumes in Figures 6 and 7 respectively. For R6G at high power, Figure 5, the location of the absorption maximum and the front of the plume travel at ~4.3 m/s and ~6 m/s respectively for the first ~0.4 ms. They gradually slow to ~1.3 m/s and ~1.7 m/s. At low power, the location of the absorption maximum and the front for the R6G plume, Figure 4, travel at ~2.6 m/s and ~5.2 m/s respectively. They gradually slow to ~1.4 m/s and ~1.7 m/s. Lateral diffusion velocities for Figures 4 and 5 are ~1.5 m/s and ~1.3 m/s respectively. Based on these observations we can conclude that R6G desorbs with greater kinetic energy, probably as a result of the larger initial absorption coefficient, and that power density, as expected, influences plume expansion rates.

The following parameters were used to roughly calculate the expected average absorbance using Beer's law: the estimated desorbed mass, the solution phase molar absorptivity, the volume over which absorbance occurs, and the pathlength (based on the vaporization line assuming no longitudinal diffusion). The calculated values were compared to those observed indicating destruction of the order of ~65% and ~75% for the NR plumes and ~80% and ~95% for the R6G plumes at low and high power

respectively. If instead the vapor phase absorptivity for R6G at ~450°C (26) is used, one estimates destruction of the order of ~88% and ~98% at low and high power respectively.

In conclusion, this imaging system allows the direct observation and mapping of the desorption of large thermally labile organic molecules. We can record how the signal grows from just a trace of absorption in the first 100 μs to a peak at ~500 μs followed by a gradual diffusion vertically and horizontally. Fragmentation of the chromophore appears to occur in the very early stages of desorption and the extent of fragmentation is dependent on both vaporization power density and sample absorptivity. The use of much lower power densities should decrease the extent of chromophore destruction. For these films in the nitrocellulose matrix, the power densities used were the minimum needed to completely desorb the irradiated area. By not using the matrix, lower powers can be used, but film uniformity suffers.

REFERENCES

1. Brech, F.; Cross, L. Appl. Spectrosc. 1962, 16, 59.

2. Burgess, D. R., Jr.; Hussla, I.; Stair, P. C.; Viswanathan, R.; Weitz, E. Rev. Sci. Instrum. 1984, 11, 1771-1776.

3. Beuhler, R. J.; Flanigan, E.; Greene, L. J.; Friedman, L. J. Am. Chem. Soc. 1974, 96, 3990-3999.

4. Posthumus, M. A.; Kistemaker, P. G.; Meuzelaar, H. L. C.; Ten Noever de Brauw, M. C. Anal. Chem. 1978, 50, 985-991.

5. Li, L.; Lubman, D. M. Anal. Chem. 1987, 59, 2538-2541.

6. Zhu, J.; Yeung, E. S. Anal. Chem. 1989, 61, 1906-1910.

7. Imasaka, T.; Tanaka, K.; Ishibashi, N. Anal. Chem. 1990, 62, 374-378.

8. Houk, R. S. In Analytical Applications of Lasers; Piepmeier, E. H., Ed.; Wiley: New York, 1986, Chapter 18.

9. van der Peyl, G. J. Q.; Isa, K.; Haverkamp, J., Kistemaker, P. G. Int. J. Mass Spectrom. Ion Phys. 1983, 47, 11-14.

10. Cotter, R. J.; Tabet, J.-C. Int. J. Mass Spectrom. Ion Phys. 1983, 53, 151-166.

11. Land, D. P.; Tai, T-L., Lindquist, J. M.; Hemminger, J. C.; McIver, R. T., Jr. Anal. Chem. 1987, 59, 2924-2927.

12. Lubman, D. M.; Kronick, M. N. Anal. Chem. 1982, 54, 660.

13. Amster, I. J.; Land, D. P.; Hemminger, J. C.; McIver, R. T., Jr. Anal. Chem. 1989, 61, 184-186.

14. Li, L.; Lubman, D. M. Appl. Spectrosc. 1989, 43, 543-549.

15. Karas, M.; Bahr, U.; Ingendoh, A.; Hillenkamp, F. Angew. Chem. Int. Ed. Engl. 1989, 28, 760-761.

16. Nelson, R. W.; Rainbow, M. J.; Lohr, D. E.; Williams, P. Science, 1989, 246, 1585-1587.

17. Brand, J. L., George, S. M. Surf. Sci. 1986, 167, 341-362.

18. Karas, M.; Bachmann, D.; Hillenkamp, F. Anal. Chem. 1985, 57, 2935-2939.

19. Spengler, B.; Karas, M.; Bahr, U.; Hillenkamp, F. J. Phys. Chem. 1987, 91, 6502-6506.

20. Huie, C. W.; Yeung, E. S. Appl. Spectrosc. 1986, 40, 863.

21. Yappert, M. C.; Kimbrell, S. M.; Yeung, E. S. Appl. Opt. 1987, 26, 3536-3541.

22. Lekavich, J. Lasers & Appl. 1986, 59-64.

23. Wilk, Z. A.; Somayajula, K. V.; Sharkey, A. G.; Hercules, D. M. Anal. Chem. 1988, 60, 2338-2346.

24. Steenhoek, L. E.; Yeung, E. S. Anal. Chem. 1981, 53, 528-532.

25. Vastola, F. J.; Pirone, A. J. Adv. Mass Spectrom. 1968, 4, 107.

26. Sakurai, T.; de Winter, H. G. J. Appl. Phys. 1975, 46, 875-878.

GENERAL SUMMARY

Three methods of characterizing particle distributions in laser-generated plumes with good temporal and spatial resolution have been shown. At high particle production, sufficient scattering and absorption allows particle concentrations to be measured in transmission mode. Measurement of particle sizes in laser-generated plumes was demonstrated using the polarization ratio and the dissymmetry ratio of scattered light based on the Mie scattering theory. Good estimates of sizes were found with good spatial and temporal resolution. Large particles were seen as arising directly from the surface and from condensation. Both methods provide good size analysis for transient events. More reliable and exact size measurements can be done by combining the methods and by using theoretical values for nonhomogeneous size distributions. Though, this would increase the number of detectors, complicating the experiment. If the polarization of the probe beam could be modulated at a high rate (~10 MHz) then two detectors, one each at 135° and 45°, could be used with a two channel digitizer. The detectors would alternately record ι_1 and ι_2 for both angles providing four independent measurements of particle size, the dissymmetry ratio for ι_1 and ι_2 and the polarization ratio at 45° and at 135°. Four measurements of particle size would aid size determination in systems where the particle size is in the multivalued region for a single measurement. This system would have timing complications between the digitizer and the polarization modulator, but it would simplify the size measurements by only requiring two detectors and two digitization

channels.

A method for two-dimensional mapping of the desorption of large organic dyes was demonstrated. The dyes continue to desorb after the laser vaporization pulse. The observation of a consistent gradual increase in dye concentration in the plume indicates that the majority of the fragmentation appears to occur at the very early stages, <100 μs, of the desorption process. Fragmentation of the dye molecules was found to depend on absorptivity by the sample at the vaporization wavelength and on power density. Sufficient temporal and spatial resolution in the imaging system allowed the observation of the desorption at its early stages.

Coupling the light scattering techniques for particle size analysis and the molecular absorption method for detection of absorbing organic molecules with acousto-optic laser beam deflection provided good spatial and temporal resolution for real-time imaging of the plasma. Application of this imaging method allows the study of individual laser and sample parameters and their influence on desorption and fragmentation.

REFERENCES

1. Kwong, H. S.; Measures, R. M. Anal. Chem. 1979, 51, 428-432.

2. Andersen, C. A. Microprobe Analysis; Wiley: New York, 1973.

3. Maiman, T. H. Phys. Rev. Lett. 1960, 4, 564.

4. Brech, F.; Cross, L. Appl. Spectrosc. 1962, 16, 59.

5. Fitzgerald, R. In Microprobe Analysis; Andersen, C. A., Ed.; Wiley: New York, 1973; Chapter 1.

6. Robinson, C. F. In Microprobe Analysis; Andersen, C. A., Ed.; Wiley: New York, 1973; Chapter 16.

7. Southon, M. J.; Witt, M. C.; Harris, A; Wallach, E. R.; Myatt, J. Vacuum 1984, 34, 903-909.

8. Moenke, H.; Moenke-Blankenburg, L. Einführung in die Laser-Mikro-Emissionsspektralanalyse, 2. Auflage; Akademische Verlagsgesellschaft Geest & Portig KG: Leipzig, German Democratic Republic, 1968; 4th Ed., Laser Microspectrochemical Analysis, Adam Hilger: London, England, and Crane, Russak: New York, 1973.

9. Moenke-Blankenburg, L. Laser Microanalysis; Wiley: New York, 1989.

10. Opauszky, I. Pure Appl. Chem. 1982, 54, 879-887.

11. Belousov, V. I. Zh. Anal. Khim. 1984, 39, 909-927.

12. Laqua, K. In Analytical Laser Spectroscopy; Omenetto, N., Ed.; Wiley: New York, 1979; Chapter 2.

13. Dittrich, K.; Wennrich, R. Prog. Anal. Atom. Spectrosc. 1984, 7, 139-198.

14. Piepmeier, E. H. In Analytical Applications of Lasers; Piepmeier, E. H., Ed.; Wiley: New York, 1986; Chapter 19.

15. Conzemius, R. J.; Capellen, J. M. Int. J. Mass Spectrom. Ion Phys. 1980, 34, 197-271.

16. Houk, R. S. In Analytical Applications of Lasers; Piepmeier, E., Ed.; Wiley: New York, 1986; Chapter 18.

17. Mossotti, V. G.; Laqua, K.; Hagenah, W.-D. Spectrochim. Acta 1967, 23B, 197-206.

18. Rasberry, S. D.; Scribner, B. F.; Margoshes, M. Appl. Opt. 1967, 6, 81-93.

19. Carr, J. W.; Horlick, G. Spectrochim. Acta 1982, 37B, 1-15.

20. Plieninger, T.; Schaeffer, O. A. Proceeding of the 7th Lunar Science Conference, Houston, TX, March 15-19, 1976. Volume 2, Petrogenetic studies of Mare and Highland Rocks, Pergamon: New York, 1976; 2055-2066. Geochim. Cosmochim. Acta, Suppl. 7.

21. Kohler, V. L.; Harris, A.; Wallach, E. R. In Microbeam Analysis-1986; Romig, A. D.; Chambers, W. F., Eds.; San Francisco: San Francisco, 1986; pp 467-470.

22. Runge, E. F.; Bonfilio, S.; Bryan, F. R. Spectrochim. Acta 1966, 22, 1678-1680.

23. Li, L.; Lubman, D. M. Anal. Chem. 1989, 61, 1911-1915.

24. Arrowsmith, P. Anal. Chem. 1987, 59, 1437-1499.

25. Wennrich, R.; Dittrich, K. Spectrochim. Acta 1982, 37B, 913-919.

26. Ko, J. B.; Sdorra, W.; Niemax, K. Fresenius Z. Anal. Chem. 1989, 335, 648-651.

27. Quentmeier, A.; Sdorra, W.; Niemax, K. Spectrochim. Acta 1990, 45B, 537-546.

28. Chen, G.; Yeung, E. S. Anal. Chem. 1988, 60, 2258-2263.

29. Huie, C. W.; Yeung, E. S. Anal. Chem. 1986, 58, 1989-1993.

30. Measures, R. M.; Kwong, H. S. Appl. Opt. 1979, 18, 281-286.

31. Talmi, Y.; Sieper, H. P.; Moenke-Blankenburg, L. Anal. Chim. Acta 1981, 127, 71-85.

32. Treytl, W. J.; Orenberg, J. B.; Marich, K. W.; Saffir, A. J.; Glick, D. Anal. Chem. 1972, 44, 1903.

33. Felske, A.; Hagenah, W.-D.; Laqua, K. Spectrochim. Acta 1972, 27B, 295.

34. Möde, U. Ph.D. Thesis, Münster, 1970.

35. Leis, F. Ph.D. Thesis, Düsseldorf, 1976.

36. Mitchell, P. G.; Sneddon, J.; Radziemski, L. Appl. Spectrosc. 1987, 41, 141-148.

37. Ishizuka, T.; Uwamino, Y. Spectrochim. Acta 1983, 38B, 519-527.

38. Kántor, T.; Pólos, L.; Fodor, P.; Pungor, E. Talanta 1976, 23, 585-586.

39. Bondybey, V. E.; English, J. H. J. Chem. Phys. 1981, 74, 6978-6979.

40. Mayo, S.; Lucatorto, T. B.; Luther, G. G. Anal. Chem. 1982, 54, 553-556.

41. Zhu, J.; Yeung, E. S. Anal. Chem. 1989, 61, 2557-2562.

42. Fenner, N. C.; Daly, N. R. Rev. Sci. Instrum. 1966, 37, 1068-1070.

43. Hercules, D. M.; Day, R. J.; Balasanmugam, K.; Dang, T. A.; Li, C. P. Anal. Chem. 1982, 54, 280A-305A.

44. Zhu, J.; Yeung, E. S. Anal. Chem. 1989, 61, 1906-1910.

45. Kubis, A. J.; Somayajula, K. V.; Sharkey, A. G.; Hercules, D. M. Anal. Chem. 1989, 61, 2516-2523.

46. Neuninger, H. Arch. Kriminol. 1969, 144, 121.

47. Petrakiev, A.; Samov, A.; Dimitrov, G. Jenaer Rundsch. 1971, 250.

48. Buravlev, J. M.; Nadeshda, B. P.; Babanskaja, L. N. Zavod. Lab. 1974, 140, 165.

49. Karyakin, A. V.; Akhmanova, M. V.; Kaigorodov, V. A. Zh. Anal. Khim. 1965, 20, 145.

50. De Waele, J. K.; Vansant, E. F.; Van Espen, P.; Adams, F. C. Anal. Chem. 1983, 55, 671-677.

51. Peppers, N. A.; Scribner, E. J.; Alterton, L. E.; Honey, R. C.; Beatrice, E. S.; Harding-Barlow, I.; Rosan, R. C.; Glick, D. Anal. Chem. 1968, 40, 1178-1182.

52. Posthumus, M. A.; Kistemaker, P. G.; Meuzelaar, H. L. C.; Ten Noever de Brauw, M. C. Anal. Chem. 1978, 50, 985-991.

53. Karas, M.; Bahr, U.; Ingendoh, A.; Hillenkamp, F. Angew. Chem. Int. Ed. Engl. 1989, 28, 760.

54. Libenson, M. N.; Romanov, G. S.; Imas, Y. A. Zh. Tekh. Fiz. 1968, 38, 1116 [Sov. Phys.-Tech. Phys. 1969, 13, 925].

55. Klocke, H. Spectrochim. Acta 1969, 24B, 263.

56. Basov, N. G.; Boiko, V. A.; Krokhin, O. N.; Semeno, O. G.; Sklizkov, G. V. Zh. Tekh. Fiz. 1968, 38, 1973 [Sov. Phys.-Tech. Phys. 1969, 13, 1581].

57. Krokhin, O. N. In Laser Handbook Vol. 2; Arecchi, F. T.; Schulz-Dubois, E. O., Eds.; North-Holland: Amsterdam, 1972; p. 1372.

58. Carroll, P. K.; Kennedy, E. T. Contemp. Phys. 1981, 22, 61.

59. Hein, S. J.; Piepmeier, E. H. Trends Anal. Chem. 1988, 7, 137-142.

60. Ready, J. F. Effects of High-Power Laser Radiation; Academic: New York, 1971.

61. Piepmeier, E. H.; Malmstadt, H. V. Anal. Chem. 1969, 41, 700.

62. Leis, F.; Sdorra, W.; Ko, J. B.; Niemax, K. Mikrochim. Acta [Wien] 1989, II, 185-199.

63. Sdorra, W.; Quentmeier, A.; Niemax, K. Mikrochim. Acta [Wien] 1989, II, 201-218.

64. Allemand, C. D. Spectrochim. Acta 1972, 27B, 185-204.

65. Colin, C.; Durand, Y.; Floux, F.; Guyot, D; Langer, P.; Veyrie, P. J. Apol. Phys. 1968, 29, 2991.

66. Scott, R. H.; Strasheim, A. Spectrochim. Acta 1970, 25B, 311-322.

67. Bykovskii, Yu. A.; Degtyarenko, N. N.; Elesin, V. F.; Kozyrev, Yu. P.; Sil'nov, S. M. Sov. Phys. JETP 1971, 33, 706.

68. Basov, N. G.; Boiko, V. A.,; Gribkov, V. A.; Zakharov, S. M.; Krokhin, O. N.; Sklizkov, G. V. Sov. Phys. JETP, 1972, 34, 81.

69. Fedosejeus, R.; Richardson, M. C. Appl. Phys. Lett., 1975, 27, 115.

70. Malvezzi, A. M.; Jannitti, E.; Tondello, G. Optics Commun. 1975, 13, 307.

71. Colombant, D.; Tonon, G. F. J. Apol. Phys. 1973, 44, 3524.

72. Galanti, M.; Peacock, N. J. J. Phys. B 1975, 8, 2427.

73. Basov, N. G.; Boiko, V. A.; Voinov, Yu. P.; Kononov, E. Ya.; Mandel'shtam, S. L.; Sklizkov, G. V. ZhETP Pis'ma 1967, 5, 177-180.

74. Chen, G.; Yeung, E. S. Anal. Chem. 1988, 60, 864-868.

75. Pang, H. M.; Yeung, E. S. Anal. Chem. 1989, 61, 2546.

76. Pang, H. M.; Yeung, E. S. Appl. Spectrosc. 1990, 44, 871.

77. Pang, H. M.; Yeung, E. S. Appl. Spectrosc. 1989, 44, 1218-1220.

78. Steenhoek, L. E.; Yeung, E. S. Anal. Chem. 1981, 53, 528.

79. Huie, C. W.; Yeung, E. S. Spectrochim. Acta 1985, 40B, 1255-1258.

80. Huie, C. W.; Yeung, E. S. Appl. Spectrosc. 1986, 40, 863-868.

81. Yappert, M. C.; Kimbrell, S. M.; Yeung, E. S. Appl. Opt. 1987, 26, 3536-3541.

82. Lekavich, J. Lasers and Applications 1986, April, 59.

83. Rohlfing, E. A. J. Chem. Phys. 1988, 89, 6103.

84. Arrowsmith, P.; Hughes, S. K. Anal. Chem. 1988, 42, 1231.

85. Barth, H. G.; Sun, S-T. Anal. Chem. 1989, 61, 143R-152R.

86. Barth, H. G. Modern Methods of Particle Size Analysis; Wiley: New York, 1984.

87. Rayleigh, Lord Phil. Mag. 1871, 41, 107, 274, and 447 (Sci. Papers 8 and 9.

88. Mie, G. Ann. Physik. 1908, 25, 377.

89. Logan, N. A. In Selected Papers on Light Scattering; Kerker, M., Ed.; SPIE-The International Society for Optical Engineering: Bellingham, Washington, 1988; pp 3-15.

90. Stratton, J. A. Electromagnetic Theory; McGraw-Hill: New York, 1941.

91. van de Hulst, H. C. Light Scattering by Small Particles; Dover: New York, 1981.

92. Kerker, M. The Scattering of Light and Other Electromagnetic Radiation; Academic Press: New York, 1969.

93. Araya, T.; Matsunawa, S.; Katayama, S.; Hioki, S.; Ibaraki, Y.; Endo, Y. U.S. Patent 4,619,691, 1986.

94. Groves, M. J. In Modern Methods of Particle Size Analysis; Barth, H. G., Ed.; Wiley: New York, 1984; Chapter 2.

95. Sinclair, D.; La Mer, V. K. Chem. Rev. 1949, 44, 245.

96. Meehan, E. J; Beattie, W. H. J. Phys. Chem. 1960, 64, 1006.

ACKNOWLEDGEMENTS

I would like to thank Dr. Edward S. Yeung, my major professor, for his guidance in this research and for his confidence in me.

For their assistance on the Fortran programs for the Mie calculations, I would like to thank Steve Woodruff and Warren Wiscombe. I would like to thank Dr. Keith Woo and his group for the use of their uv-vis spectrometer throughout the dye studies.

For their financial support, I would like to thank the Chemistry Department, Ames Laboratory, and BP-America. This work was performed at Ames Laboratory under contract no. W-7405-eng-82 with the U. S. Department of Energy. The United States government has assigned the DOE Report number IS-T 1516 to this thesis.

I thank the research group members and their families for their assistance both in and out of lab, but mostly for making the group fun to be a part of. To the many friends I have met while in Iowa, you will make me smile when I think back on these years.

I thank my grandmother, Leone Irwin, for her assistance when I first arrived in Ames. Thank you for helping me find a place to stay and for introducing me to my other relatives who I have not known for many years.

I would like to thank my parents, Ted and Shirley Marshall, for their love and encouragement, and for teaching me to believe in myself.

Lastly, for his love, companionship, and patience, even when I dragged him to Iowa for five years, I give all my love to my husband, Keith.